Title: **Secondary ossification centers evolved to make endochondral bone growth possible under the weight-bearing demands of a terrestrial environment.**

Authors: Meng Xie[1], Pavel Gol'din[2], Anna Nele Herdina[1], Jordi Estefa[3], Ekaterina V Medvedeva[6], Lei Li[1], Phillip T Newton[1,4], Svetlana Kotova[6,7], Boris Shavkuta[6,13], Aditya Saxena[17], Lauren T Shumate[15], Brian Metscher[16], Karl Großschmidt[18], Shigeki Nishimori[15], Anastasia Akovantseva[6,13], Irene Linares Arregui[5], Paul Tafforeau[8], Kaj Fried[11], Mattias Carlström[1], Andras Simon[12], Christian Gasser[5], Henry M Kronenberg[15], Murat Bastepe[15], Kimberly L. Cooper[17], Peter Timashev[6,7,13], Sophie Sanchez[3,8,14], Igor Adameyko[1,10], Anders Eriksson[9], Andrei S Chagin[1,6*]

Affiliations

1. Department of Physiology and Pharmacology, Karolinska Institutet, Stockholm, Sweden
2. Department of Evolutionary Morphology, Schmalhausen Institute of Zoology of NAS of Ukraine, Ukraine
3. Science for Life Laboratory and Uppsala University, Subdepartment of Evolution and Development, Department of Organismal Biology, Uppsala, Sweden
4. Department of Women's and Children's Health, Astrid Lindgren Children's Hospital, Karolinska University Hospital, Sweden
5. Department of Solid Mechanics, KTH Royal Institute of Technology, Stockholm, Sweden
6. Institute for Regenerative Medicine, Sechenov University, Russia
7. Semenov Institute of Chemical Physics, Russia
8. European Synchrotron Radiation Facility, Grenoble Cedex, France
9. Department of Mechanics, KTH Royal Institute of Technology, Stockholm, Sweden
10. Department of Molecular Neurosciences, Medical University of Vienna, Austria
11. Department of Neuroscience, Karolinska Institutet, Stockholm, Sweden
12. Department of Cell and Molecular Biology, Centre of Developmental Biology for Regenerative Medicine, Karolinska Institute, Stockholm, Sweden
13. Institute of Photonic Technologies, Research center "Crystallography and Photonics", Russia
14. Sorbonne Université – CR2P – MNHN, CNRS, UPMC, Paris, France
15. Endocrine Unit, Department of Medicine, Massachusetts General Hospital and Harvard Medical School, Boston, U.S.A.
16. Department of Theoretical Biology, University of Vienna, Austria
17. Division of Biological Sciences, University of California San Diego, USA
18. Bone and Biomaterials Research, Center for Anatomy and Cell Biology, Medical University of Vienna, Vienna, Austria

*Corresponding author:
Andrei S Chagin andrei.chagin@ki.se

Abstract

The growth of long bones occurs in narrow discs of cartilage, called growth plates that provide a continuous supply of chondrocytes subsequently replaced by newly formed bone tissue. These growth plates are sandwiched between the bone shaft and a more distal bone structure called the secondary ossification center (SOC). We have recently shown that the SOC provides a stem cell niche that facilitates renewal of chondro-progenitrors and bone elongation. However, a number of vertebrate taxa, do not have SOCs, which poses intriguing questions about the evolution and primary function of this structure. Evolutionary analysis revealed that SOCs first appeared in amniotes and we hypothesized that this might have been required to meet the novel mechanical demands placed on bones growing under weight-bearing conditions. Comparison of the limbs of mammals subjected to greater or lesser mechanical demands revealed that the presence of a SOC is associated with the extent of these demands. Mathematical modelling with experimental validation showed that the SOC reduces shear and normal stresses within the growth plate; while relevant biological tests revealed that the SOC allows growth plate chondrocytes to withstand a six-fold higher load before undergoing apoptosis. Hypertrophic chondrocytes, the cells primarily responsible for bone elongation, were the most sensitive to loading, probably due to their low Young's modulus (as determined by atomic force microscopy). Our present findings indicate that the primary function of the evolutionary delineation of epiphyseal cartilage into spatially separated growth plates was to protect hypertrophic chondrocytes from the pronounced mechanical stress associated with weight-bearing in a terrestrial environment.

Main text

Long bones grow longitudinally via an epiphyseal growth plate, a tiny structure containing chondrocytes that proliferate, align in the longitudinal direction and then enlarge several-fold (hypertrophy). Thereafter, these hypertrophic chondrocytes undergo apoptosis or trans-differentiation (*1*), leaving their calcified extracellular matrix as a scaffold on which invading blood vessels and osteoblasts form new bone tissue. This process of bone growth on a cartilage template is referred to as endochondral bone formation. Recent 3D microanatomical characterization of the 380-million-year-old lobe-finned fish *Eusthenopteron(2)* revealed longitudinally oriented trabeculae within the shaft of their humeri (Fig. 1, A), a strong indication that endochondral ossification facilitated bone elongation in stem tetrapods in a manner similar to present-day mammals (Fig. 1, A to C) (*2, 3*).

In humans, as well as in the experimental animals employed most commonly to study bone growth (i.e., mice, rats and rabbits), the growth plate is separated from the articular cartilage by a bony fragment, the secondary ossification center (SOC). This skeletal element, formed during early postnatal development, splits the initially contiguous cartilaginous element into two independent structures, the growth plate and articular cartilage (Fig. S1, A and B) (*4*). Our recent findings indicate that the SOC provides a stem cell niche where chondro-progenitors within the growth plate can renew themselves and thereby maintain linear growth (*5*). However, the SOC

is absent in several vertebrate taxa, such as Chelonians, Crocodilians and Urodeles (*6, 7*) (as an example, salamander cartilage is shown in Fig. S1, C and D). This observation poses an intriguing question about the evolutionary origin of the SOC and primary cause of its development.

Evolutionary analysis revealed that SOCs first appeared in the long bones of amniotes and are present in all synapsids (including mammals) (Fig. 1, D). Some stem mammals may have evolved a SOC [i.e., *Niassodon(8)* (Fig. 1, D)], but most did not (*9, 10*). Among sauropsids bone ossification is widely diversified: SOCs form in squamates (lizards) and calcified secondary centers (SCs) in sphenodontids (Fig. 1, D), whereas Chelonians (turtles and tortoises) and crocodilians do not possess an SOC(*7*). Instead, in these organisms the bone marrow protrudes unevenly into epiphyseal cartilage, leaving hypertrophic chondrocytes between and forming trabecular bones on sides of these protrusions (*7*).

The long bones of some birds can form a SOC (e.g., proximal epiphysis of the tibiotarsus in the sparrow, Fig. S2), but most ossify their long bones without such a structure (*11*). In both cases, trabecular protrusions extend towards the epiphysis (*7, 12*) in a manner that in principle resembles the protrusions of marrow in crocodilians and chelonians, but more organized, narrowed and extended protrusions. The bones of non-avian dinosaurs appear to have been organized in a manner similar to birds (i.e., extended protrusions (*9, 10*)), to the best of our knowledge with no reports of SOCs in these groups. The absence of SOCs in anamniotes and its appearance in different orders of amniotes indicate evolutionary convergence and suggests that SOCs might play an important and previously unexplored adaptive role in the functioning of the appendicular skeleton.

Anamniotes undergo their juvenile growth in an aquatic environment, with amniotes being the first organisms to spend their entire lifecycle on land. Such a change in habitat poses an engineering challenge to the skeleton, which must be rigid enough to bear the weight of the body during wide-ranging movements of the joints and yet flexible enough to allow bone growth. Accordingly, we reasoned that the SOC might help meet this challenge.

To examine a potential association between the SOC and mechanical demands, we first looked at the skeletal development of Chiroptera (bats), who use their extremities in a highly specialized manner. The newborn pups must cling to their mother or to the roost during their mothers' flights for foraging or relocation. Thus, the feet and thumbs (1st finger) of the wing are expected to be subjected to greater initial weight-bearing demands than the long wing bones, which start to be utilized only after about 2-3 weeks of age (*13-16*). Accordingly, we compared ossification of the feet and thumbs to that of the other bones of the wing. We found that in newborn bat pups, development of the SOCs in the hindlimbs and thumbs is much more advanced than in the wings (Fig. 1, E and Video S1), in line with the heavy mechanical demands described above. This difference was particularly pronounced in the case of autopods, where the feet and thumb are heavily ossified, while other bones of the wing exhibit no SOC at all (Fig. 1, F to G). This differential pattern of ossification was apparent during ontogenesis in the entire Chiroptera order (Fig. 1, H and I, summary of 6 species for

which ontogeny data were available to us) and primary data on all 13 species analyzed are presented (Supplementary data file 1). The Chiroptera species differ extensively with respect to their foraging and roosting habits, the behavior of their young, litter size, and lifespan (*17-21*), which probably resulted in a certain amount of variation.

Interestingly, the SOCs in the feet and the thumbs of some species of bats are well-developed even prior to birth (Supplementary data file 1) and the pups of certain species (*Mops condylurus*, *Artibeus jamaicensis*, *Megaloglossus woermani* and *Rousettus celebensis*) are born with feet of nearly adult size (*17, 19*) (see also Fig. 1F for *A. jamaicensis*). Use of the wings (other than the thumb) begins much later than that of the feet and a SOC develops in the wing bones late in the juvenile period. Thus, these comparisons reveal a clear association between mechanical demands and the time at which the SOC is formed. Interestingly, the presence of the SOC in the embryonic feet and thumb suggests that a genetic program governs development of this structure preceding the mechanical demands.

To verify this association between the level of ossification and mechanical demands in an unrelated order, we examined development of the SOC in a bipedal three-toed jerboa (*Jaculus jaculus*) belonging to the family of Dipodoidea rodents. The young employ their front limbs only for crawling during the first 2 weeks of postnatal life and start using their hind limbs (become quadrupedal) at 3 weeks of age, becoming fully bipedal at 4 weeks of age (Video S3) and (*22*). Consistent with the associated mechanical demands, the SOC formed in the front limbs significantly before the hind limbs (Fig. 1K, L, and Fig. S3). Interestingly, development of the SOC in mice and rats also coincides with the transition from crawling to walking (Fig. S1, A and B).

This same line of reasoning suggests that the evolutionary movement of mammals from land to water, such as that of the cetaceans (whales) with their streamlined body and flippers (Fig. S4, A), might have led to the loss of this specialized structure. In early cetaceans from the Eocene era (56-33.9 Mya), the epiphyseal plates of the forelimbs are structurally similar to those of terrestrial mammals, as evident in *Maiacetus inuus (23)* and *Dorudon atrox (24)* (Fig. S4, B1 and B2, respectively). However, the SOCs in the metacarpals and phalanges in extant baleen whales of the Balaenopteridae family are extremely small, although well-developed in the distal radius and ulna (Fig. S4, B3). The Balaenidae family demonstrates the most advanced limb transformation, with extreme reduction of the size of the SOC in the distal radius, ulna and metacarpals; unusually small or even missing carpal elements; and a fibrocartilaginous structure intermediate to that of the zeugopodium and metacarpals (Fig. S4, B4).

Toothed whales from the Miocene era to the present demonstrate more diversified secondary ossification. Iniidae (Amazon River dolphins) do not have distinct epiphyseal plates, but rather multiple small SOCs (Fig. S4, B6). SOCs are present in both Platanistidae and certain Delphinoidea (Fig. S4, B5), whereas the SOCs of Ziphiidae and the narwhal *Monodon monoceros* (Delphinapteridae), are reduced in size (Fig. S4, B7). In another member of Delphinapteridae, the beluga whale *Delphinapterus leucas*, X-ray examination revealed only remnants of a SOC in the metacarpals and phalanges (Fig. S4, D). Finally, the most advanced epiphyseal

transformation is seen in the killer whale *Orcinus orca* (Delphinidae) (Fig. S4, B8) and sperm whale *Physeter catodon (25, 26)* (Fig. S4, B10), where the size of the SOCs of the distal radius, ulna and metacarpals is extremely reduced (sometimes even absent) and a fibrocartilaginous structure forms in the carpal area (Fig. S4, B8,10). A CT scan revealed complete absence of the SOC in *Orcinus orca* (Fig. 1, J and Video S2), as confirmed by radiography (Fig. S4, C). Thus, the return of cetaceans to the aquatic environment was associated with a reduction in the size of their SOCs, indeed, with complete loss of this structure in some species.

These evolutionary and comparative observations on unrelated animals suggest that appearance of the SOC occurred in relation to mechanical demands imposed on skeletal elements. However, alternative explanations, such as temporal differences in maturation of the growth plate, cannot be definitely excluded by such associative studies. We therefore performed a series of modelling and functional experiments to further test for our hypothesis.

To explore the potential effects of the SOC on the distribution of mechanical stress within the epiphyseal cartilage, we applied finite element analysis (FEA), employing a modification of the model developed by Carter and co-workers (*27, 28*) (Fig. 2, A, see the Methods section for details). For modelling local forces, octahedral shear stress was considered to be the most significant element of stress on chondrocytes (*28*). Our FEA revealed that the presence of a SOC reduces the extent to which octahedral shear stress (associated with either a vertical or angled load, the latter mimicking locomotion) is distributed to the epiphyseal plate (Fig. 2, A), even with a supra-physiological load (Fig. S5, A).

Our FEA model also predicted that a SOC significantly enhances the stiffness of the entire epiphyseal structure (note the tissue deflection in Fig. 2, A and Fig. S5, A), thereby preventing severe distortion and consequent instability of this structure during locomotion. To test this experimentally, we employed tibia bones from 10-day-old rats and 30-day-old mice, which at these time-points are comparable in size and shape, as well as the mechanical properties of their cartilage (Fig. S5, B and C), although the rat tibia has not yet developed a SOC (SOC-), whereas mice tibia have (SOC+) (Fig. S1, A and B). To test FEA predictions we applied various dynamic loads to these SOC± bones. As predicted, the SOC improved their stiffness in response to both vertical and angled loads (Fig. 2, B and C and Fig. S5, D to I). Although confounding experimental variables cannot be fully excluded in this SOC± modelling system even despite comparable size, shape and mechanical properties of the bones, concurrence of mathematical predictions and physical tests further validates the model.

Thus, the SOC provides additional stiffness, while simultaneously reducing octahedral shear stress on the epiphyseal growth plate. Why might such protection be important at the cellular level? To address this question, we cultured bones exposed to different loads for 48 hours under previously optimized conditions (*29*) to allow cellular responses to develop. Growth plate chondrocytes appeared to be highly sensitive to load, with 40% dying upon application of a 1N load (as revealed by propidium iodide (PI) staining). At the same time, the SOC clearly protected these cells, allowing them to withstand a load an order of magnitude higher (Fig. 2, F and G and

Fig. S6). The unfavorable effect of loading was confirmed by the reduction in the expression of chondrocyte markers, including parathyroid hormone-related peptide (PTHrP), Indian hedgehog (Ihh) (Fig. 2, D and E) and Collagen type X (Col X) (Fig. S5, K and L).

Cells frequently undergo programmed cell death (i.e., apoptosis) under unfavorable conditions. To test the hypothesis that in response to excessive mechanical load chondrocytes die by apoptosis, we first performed the TUNEL assay to detect fragmented DNA, a hallmark of apoptotic nuclei and found that growth plate chondrocytes in bones that lacked a SOC became apoptotic in response to high loads (Fig. 2, H to J and see Fig. S5, J for the baseline control). In addition, Caspase-3, a protease that executes apoptosis, was activated upon loading (Fig. 2, K). To further explore the underlying mechanism, we assessed the activity of the Yes-associated protein 1/Tafazzin (YAP/TAZ) signaling pathway, which is well-known to be involved in mechano-sensing (*30*) and can promote apoptosis via the tumor suppressor protein, p73 (*31*). The levels and nuclear translocation of both the YAP (Fig. S7, A and Fig. S9, K and L) and p73 proteins (Fig. S7, B) were enhanced by loading and the overlapping distribution of these two proteins further supported activation of this signaling pathway (Fig. S7, C). Taken together, the caspase-dependent apoptosis, probably via the YAP-p73 pathway, appears to be triggered in vulnerable epiphyseal chondrocytes in the absence of a protective SOC.

We noticed that this cell death was distributed unevenly along the longitudinal axis, being more pronounced in the hypertrophic zone (Fig. 3, A to D and Fig. 2, J). The levels of active caspase-3, YAP and p73 were also higher in this zone than in the resting/proliferative zone (Fig. 3, E to H and Fig. S8, A to D). In bones lacking a SOC, hypertrophic chondrocytes died with a load as low as 0.2N (Fig. 3, I), whereas in the presence of this structure cell death occurred only with loads of 5N under vertical load and 3N under angled load (Fig. 3, A to D). Within this range of loading no effect on chondrocyte proliferation could be observed (Fig. S8, E and F), suggesting that hypertrophic chondrocytes are particularly sensitive to loading. The protective effect of a SOC on this cellular population was especially strong, allowing them to withstand a 25-fold greater load (0.2N versus 5N for vertical load).

This highly efficient protection prompted us to modulate the size of the SOC in age-matched individuals, with a less sensitive, but more physiological setting. We recently reported that development of the SOC is dependent on angiogenesis and can be delayed by blocking the vascular endothelial growth factor (VEGF) receptor in transgenic mice (*5*) with axitinib (*32*) within a narrow window of time beginning of P18, but not P21. Similar inhibition was observed here in wild-type mice (Fig. 3, J). Delayed development of the SOC was clearly associated with elevated apoptosis among hypertrophic chondrocytes (Fig. 3, K).

In addition, we analyzed mice characterized by limb-specific activation of the stimulatory G-protein α-subunit (Gsα) and delayed formation of the SOC (Prx-Cre:Gsα^{R201H}) (*33*). To block immediate elimination of dead hypertrophic chondrocytes by ingrowing blood vessels, we inhibited angiogenesis with axitinib as described above, which does not interfere with formation of the SOC (P21-P29, Fig. 3, K), but allows

delay elimination of hypertrophic chondrocytes (*5*). Analysis confirmed a decreased in the size of the SOC and revealed enhanced death among hypertrophic chondrocytes (Fig. S8, G and H). It must be emphasized that in both pharmacological and genetic murine models, the animals run actively, exposing their growth plates to weight-associated loads, but their body mass is lower (for axitinib-treated mice 56.6±11.2% of control and Prx-Cre:Gsα^{R201H} mice 80±6.9% of control). Thus, the increase in cell death observed may be an underestimation of the level to be expected in bones with an underdeveloped SOC subjected to normal body weight.

Intriguingly, in our SOC± model we also noticed that when loading was applied at an angle, dying hypertrophic chondrocytes were distributed unevenly, not only along the longitudinal (resting&proliferative - hypertrophic, Fig. 3), but also along medial-lateral axis. Specifically, chondrocytes on the side opposite the loading underwent more extensive apoptosis than those on the other side (Fig. 4, A to C). Similarly, the number of TUNEL-positive cells and level of YAP were also highest on the side opposite to where the load was applied (Fig. S9, C, E, G, I). Vertical loading did not affect the medial-lateral spatial distribution of cell death, thereby serving as a control (Fig. S9, A, B, D, F, H, J). A similar medial-lateral distribution of cell death was observed in mice where formation of the SOC was delayed by chondrocyte-specific ablation of the salt-induced kinase 3 (Sik3) (Col2-Cre:Sik3-FL/FL mice)(*34*) (Fig. 4, D). In these actively running animals, more hypertrophic chondrocytes on the lateral sides of the growth plate died than in the middle (Fig. 4, E).

This uneven distribution of cell death along the medial-lateral axis cannot be explained by the octahedral shear stress, since with angled loading this stress is the highest in the central region of the growth plate (Fig. 2, A). Our FEA model revealed that with angled loading, only the highest compressive principal stress (Fig. 4, F) and hydrostatic stress (Fig. S9, M and S10 for physiological and supra-physiological loads, respectively) match this medial-lateral distribution of cell death. Hydrostatic stress was not considered further, since this also increased upon vertical loading in the presence of a SOC, which therefore cannot protect against this form of stress (Fig. S9, M).

Thus, directional compressive stress appears to be harmful to chondrocytes, especially hypertrophic chondrocytes. To understand this vulnerability, we determined cell stiffness by performing atomic force microscopy (AFM) on live tissue sections (freezing sections or isolating cells might alter their stiffness (*35*)). Hypertrophic chondrocytes proved to be only a quarter as stiff as the columnar chondrocytes from which they are derived (Fig. 4, G and H). It seems likely that this lower stiffness of hypertrophic chondrocytes, in combination with their large size, render them particularly vulnerable to mechanical loading.

Long-bone elongation through endochondral bone formation has been conserved evolutionarily for at least 400±20 Mya(*2, 3*). Chondrocyte hypertrophy is a key aspect of this process, not only accounting for 59% of growth (73% with the associated ECM) (*36, 37*), but also coordinating cartilage resorption with the formation of new bone (e.g., via secretion of Ihh and VEGF) (*38*). Thus, while juvenile growth in an aqueous environment places no special demands on the mechanical properties of

hypertrophic chondrocytes, transition to land poses the mechanical stress of weight-bearing, particularly on the appendicular skeleton, which in turn might damage the hypertrophic chondrocytes and thereby preclude proper bone formation. Accordingly, SOCs can be viewed as a mechanism to preserve the evolutionary ancient process of endochondral bone formation in connection with terrestrial loading.

However, most vertebrates lack SOCs. Among terrestrial crown amniotes, the mammals and lepidosaurs have this structure, whereas non-avian dinosaurs, crocodilians and chelonians do not (Fig. 1, D). (Although some bones in some birds do develop SOCs (Fig. S2)), instead, birds and dinosaurs and, to a lesser extent, chelonian and crocodilians develop bone marrow protrusions with calcified or ossified walls that protrude deep into the epiphyseal cartilage, sequestering hypertrophic chondrocytes between them (*11, 12, 39*). Modelling this system revealed that this design relieves the hypertrophic zone in a highly efficient manner from loading-induced stress (Fig. S10). The epiphysis of chelonians and crocodilians, which deviates least from the most ancient types (*12*), probably protect the hypertrophic chondrocytes partially by the longitudinal trabecular arrangement of their metaphysis (Fig. S10) in combination with the partial reduction in load-associated stress achieved by an aquatic juvenile period or crawling. These observations suggest that amniotes appear to have addressed the same poor compatibility of hypertrophic chondrocytes with the mechanical demands of terrestrial bone growth, albeit with a different evolutionary strategy. It is interesting to emphasize that the SOC is formed at the expense of chondro-progenitors located in this same area, which should theoretically limit the potential growth of terrestrial animals with SOC structure. Expression of sonic hedgehog by cells in the SOC and development of an epiphyseal stem cell niche by this bony structure (*5*) might be secondary or parallel adaptations designed to overcome this loss of chondro-progenitors and associated limited growth potential.

In conclusion, our evolutionary observations, comparative zoology, paleontological analyses, mathematical modeling and physical tests, as well as pharmacological and genetic interventions all suggest strongly that the primary reason the SOC evolved was to shield the hypertrophic chondrocytes from the mechanical stress of weight-bearing associated with bone growth in a terrestrial environment. These observations provide evolutionary, mechanistic and functional explanations for the Hueter-Volkmann law formulated during 1862-1897, which states that "*increased mechanical compression reduces longitudinal bone growth while reduced mechanical loading increases it*"(*40*).

These novel insights concerning the primary cause for evolution of the SOC and the associated formation of a spatially defined growth plate in mammals (including humans) might influence the design of sporting activities for young people during their most active period of growth, as well as help develop new surgical strategies for the treatment of epiphyseal fractures.

Acknowledgements

This work was supported financially by the EMBO Long-Term Fellowships (MX) and grants from the Swedish Research Council (ASC: 2016-02835; SS: 2015-04335),

Karolinska Institutet (MX, ASC, LL, IA) including an SFO Stem/Regen junior grant (ASC), the Bertil Hallsten Foundation (IA), the EMBO Young Investigator Program (IA), the Åke Wiberg Foundation (IA), the Chinese Scholarship Council (LL), Stiftelsen Frimurare Barnhuset i Stockholm (PN, MX), the Museum of the Southern Jutland (PG) and the Russian Science Foundation (Grant No. 18-15-00401) (PT, BS, SK, AA), as well as by an internal start-up grant from the Sechenov University to ASC (EVM, ASC). O Lambert (IRSNB), MT Olsen (ZMUC), F Zachos (NMW), PHC Lina (Naturalis), D Kalthoff (Museum of Natural History, Stockholm, Sweden) and J. Klembara (CU) provided access to specimens in collections under their care. Synchrotron beamtime was allocated in response to a proposal accepted by the ESRF (EC203, SS; ES342, JE) and as in-house beam-time (PT). The authors thank F. Arnberg (Karolinska Institutet) and Astrid Haase (Medical University of Vienna) for the help with the micro-CT, CT and X-ray scans.

Materials and Methods

Ethics

Except for those involving AFM, all animal experiments were pre-approved by the Ethical Committee on Animal Experiments (Stockholm North Committee/ Norra Djurförsöksetiska Nämnden) or the Institutional Animal Care and Use Committee of the Massachusetts General Hospital and conducted in accordance with the provisions and guidelines for animal experimentation formulated by the Swedish Animal Agency. Animal experiments involving AFM were pre-approved by the Ethics Committee of the Sechenov First State Moscow Medical University (Moscow, Russia).

Museum collections

The museum specimens of cetaceans were examined at the Royal Belgian Institute of Natural Sciences (Brussels, Belgium), Natural History Museum Stockholm (Stockholm, Sweden) and Zoological Museum, University of Copenhagen (Copenhagen, Denmark). The specimens shown in Fig. S4, B3 to 9 were preserved naturally, B1 to 2 are the casts of unprepared articulated skeletons and the carpal area in B10 is paraffinated (orange colour) so that only ossifications on the surface can be seen. Please note that all Cetaceans analyzed were adult or sub-adult, except for one of the two sperm whales.

The museum specimens of Chiroptera were from the Naturalis Biodiversity Center (Leiden, Netherlands) and Natural History Museum Vienna (Vienna, Austria).

The humerus of *Eusthenopteron* (NRM P248d) came from the Devonian locality of Miguasha (Quebec, Canada) and is housed in the collection of the Natural History Museum (Stockholm, Sweden). The humerus of *Seymouria* (MNG 7747) came from the Permian locality of the Cutler Formation (Arroyo del Agua, North-Central New Mexico) and is housed in the collection of the Museum der Natur (Gotha, Germany). The humerus of the squirrel and the skeleton of the sparrow come from a private collection (PT).

Synchrotron scanning and 3D modeling

All these scans were performed on the beamline ID19 (European Synchrotron Radiation Facility, France) with a current of 200 mA or 16 bunch. Scanning and 3D-

modeling of the humerus of *Eusthenopteron* were performed as described earlier (*2*). The data were reconstructed by single-distance phase retrieval(*41*) based on a modified version of an algorithm described earlier (*42*), with subsequent application of an unsharp mask to the radiographs to enhance the trabecular mesh.

The humerus of *Seymouria* was imaged at a voxel size of 3.48 µm using an optical system attached to a 47-µm GGG (i.e., a gadolinium gallium garnet crystal) scintillator and a FreLON 2k14 CCD detector (*43*) with a propagation distance of 700 mm. The gap of the W150m wiggler was opened to 37 mm. The sample was imaged at 80 keV using a beam filtered with 0.25 mm tungsten and 2 mm aluminium. Under half-acquisition conditions, 4998 projections were collected over 360° with an exposure of 0.15 s. Binned images (final voxel size 6.96 µm) were reconstructed, segmented and 3D-modeled in the same manner as for *Eusthenopteron(2)*.

The scan of the humerus of *Sciurus vulgaris* was performed ath the same voxel size (3.48 µm) using the same optics (i.e. a FreLON 2k14 CCD camera and 47 µm GGG scintillator), with imaging at a propagation distance of 500 mm. The beam was filtered with 0.14 mm tungsten, 0.14 mm copper and 2.8 mm aluminium. The gap of the W150m wiggler was opened to 50 mm, resulting in an energy of 65.8keV. Under half-acquisition conditions, 4998 projections were collected over 360° with an exposure of 0.15 s.

MicroCT and X-radiography

X-ray microtomography (microCT) of *Pipistrellus pipistrellus* and other bats and X-radiography of *Delphinapterus leucas* were carried out at the Department of Theoretical Biology, Faculty of Life Sciences, University of Vienna, Austria, and CT imaging of *Orcinus orca* at the Karolinska Institutet (Stockholm, Sweden). The entire bat skeleton (Fig.1, E and Video S1) was imaged with a SkyScan 1174 (Bruker microCT; isotropic voxel size 21.7 µm, exposure 3.6 sec, averaging 4 frames, rotation step 0.39°, 360° scan, 50 kV, 8 W, tungsten x-ray source) and the resulting image segmented in Amira 6.1. The wing and foot (Fig. 1, E1 and 2) were imaged with an Xradia MicroXCT (Zeiss X-Ray Microscopy; isotropic voxel size 8.8 µm (1) and 8.5 µm (2), respectively, exposure 20 sec, rotation step 0.3°, 180° scan, 80 kV, 8 W, tungsten x-ray source) and the image again segmented in Amira (6.1). These specimens were mounted in 70% ethanol in tight-fitting tubes. The 3D measurements of the surface were performed in Amira (6.1).

Measurements and calculations of the level of ossification in Chiroptera

Bats are considered to be adult when both epiphyses of the metacarpo-phalangeal joint of the 4th finger have become fully ossified. The heights of these epiphyses and their SOCs were determined from microCT images (unpublished data) using the Fiji software or from published images of limb bones (as specified in Table S1). The height of the SOC was divided by the total height of the epiphysis (from the joint to the primary ossification center), with the ratio zero corresponding to non-ossified and the value one to fully ossified epiphysis.

In cases where only gap values were available from the literature (non-visible soft tissue between two ossified elements), the height of the gap was multiplied by 2/3

(metacarpus) or 1/3 (phalanx) to estimate the total height of the epiphyses, and the height of the SOC calculated by subtracting the height of the proximal (metacarpal) or distal (phalanx) gap from this total height.

In the case of Fig. 1, the level of ossification of wing autopods was calculated as an average of the ossification of metacarpals 2-5 and the proximal phalanges 2-5. Ossification of foot autopods was calculated as an average of the ossification of metacarpals 1-5 and the proximal phalanges 1-5. Ossification of the thumb was calculated as an average of the metacarpal and the proximal phalange. Ossification of the stylopod and zeugopod was calculated as an average of the humerus, radius, and ulna for the wings and of the femur, tibia, and fibula for the legs. The results for the proximal and distal epiphyses were combined whenever both were available.

Jerboa housing and movies

Jerboas were housed and cared for as described previously (*44*) and in accordance with UCSD Institutional Animal Care and Use Committee guidelines. The locomotion of individual pups from a single litter was filmed 7, 14, 21 and 28 days after birth in a well-lit room using an iPhone with no flash.

Preparation of Jerboa skeletons

For this purpose, we followed a protocol published previously(*45*) with minor modifications, with all steps being performed on a rocker at room temperature. Samples freshly dissected and de-skinned were first fixed in 100% ethanol for 24 hours and then treated with 100% acetone for 24 hours. Subsequently, fixed samples were stained for 3-5 days by adding 1 volume each of 0.3% alcian blue (Sigma) in 70% ethanol, 0.1% alizarin red (Sigma) in 95% ethanol and glacial acetic acid to 17 volumes 70% ethanol. Thereafter, they were rinsed twice with deionised water and destained with 1% KOH (in deionised water) until the soft tissue had cleared and skeletal elements became visible (usually 1-4 days, depending on the age of the sample). Samples were then destained in 20%, 50% and 80% glycerol diluted with 1% KOH until the desired contrast was achieved (approximately 1-2 days for each dilution), and stored and imaged in 100% glycerol at room temperature with a Leica MZ16 stereomicroscope and a ringed bright light source.

Mice and rats

30-day-old C57BL/6 mice (body weight 14.59±0.72 g) and 10-day-old Sprague Dawley rats (body weight 20±0.49 g) were purchased from Charles River Laboratories and Janvier Labs (Europe). The C57BL/6 mice used for the experiments with axitinib were purchased from Charles River Laboratories. Col2-Cre:Sik3-FL/FL mice were obtained from Dr. Henry Kronenberg, Massachusetts General Hospital. The Sik3-FL/FL mice were originally purchased from EUCOMM and the Col2-Cre mice were obtained from Richard R. Behringer, University of Texas MD Anderson Cancer Center(*46*). Prx-Cre:Gsα^{R201H} mice were generated by Dr. Murat Bastepe, Massachusetts General Hospital, as described previously(*33*).

Dissection and culturing of the tibia and femur

From both hind legs of 30-day-old mice and 10-day-old rats, the tibia and femur bones were dissected out aseptically in DMEM/F12 medium supplemented with 50 µg/ml gentamycin (dissection medium) on ice, with removal of as much surrounding tissue as

possible. The height and diameters of the top and side surfaces of the epiphysis were measured with a digital caliper. For each animal, one set of tibia and femur was used as a control and the other for treatment, with all comparisons being made on bones from the same animal.

Still in dissection medium on ice, the bones were subjected to pressure with the Instron ElectroPuls E1000 Test Instrument. Load was applied at a speed of 0.1 N per second and load/digital position curves recorded in the Bluehill 3 software. Control bones went through these same procedures, but without loading.

For culturing, bones were first washed twice in dissection medium before being placed into DMEM/F12 medium supplemented with 1 mM β-glycerophosphate, 0.2% bovine serum albumin, 50 µg/ml ascorbic acid and 50 µg/ml gentamycin for 48 hours, as described previously(*25*). Propidium iodide (stock solution at 1 mg/ml, Sigma) was added to the culture medium at a ratio of 1:50 30 minutes before termination of culturing. The tibia and femur were then fixed in 4% PFA overnight, decalcified, cleared in 30% sucrose overnight (at 4° C) and finally embedded in optimal cutting temperature (OCT) compound for frozen sectioning. When the load was applied, the plateau of the medial tibia flanked by the groove of the tibia bone was always facing in one direction and the angled pressure applied to one side of the plateau (on top of one of the grooves). When embedding in OCT for sectioning, the bone was always placed into the grid with the plateau of the medial tibia facing upward and then sectioned frontally to ensure that the pressure was properly directed during imaging.

Calculation of mechanical and material properties

Determination of the position of the bone relative to the position of its fixture yielded the deformation value. Stiffness was defined as the slope of the initial linear portion of the load-deformation curve. Stress was calculated by distributing the load equally over the top (vertical load) or side surface (angular load) of the epiphysis, assuming that both of these surfaces were oval. Strain was calculated by distributing the bone deformation equally along the height of the epiphysis. The initial linear portion of the stress-strain curve (up to 0.2% offset) was plotted together with the stress-strain curve itself in the same graph and the intersection of the line and curve defined as the 0.2% offset yield strength.

Injection of axitinib

Axitinib (Sigma) was dissolved in DMSO and injected intraperitoneally at a dose of 0.25 mg per animal per day for the C57BL/6 mice for 8 (P21 - P27) or 10 days (P18 - P27 or P21 - P30). The control animals received the same volume of DMSO alone. Transgenic Prx-Cre:Gsα^{R201H} mice and the corresponding Gsα^{R201H} controls were injected daily (0.017 mg per g of body weight) between 21 and 29 days of postnatal age to block the elimination of dead hypertrophic chondrocytes by ingrowing blood vessels. Animals were sacrificed one day after the last injection of axitinib.

TUNEL staining

30-µm sections of cultured tibia bones were treated with proteinase K (Ambion) at 10 µg/ml for 40 minutes at 37° C before applying the TUNEL reaction mix (Roche Inc.) for 90 minutes. The cells were then counter-stained with DAPI for 30 minutes.

Quantification of stained cells (PI+, TUNEL+, YAP+ etc)

For each quantification of the numbers of PI+ and TUNEL+ cells, at least three sections from each of at least three different animals were analyzed. All counting, including determination of the medio-lateral distributions of PI+, TUNEL+, Caspase-3+, p73+, YAP+ and double p73+YAP+ cells was double-blinded.

Immunofluorescent staining

30-µm sections of cultured tibia bones were blocked in 3% normal horse serum for one hour, followed by overnight incubation with primary antibodies against cleaved caspase 3 (1:500) (Cell Signaling), YAP (1:50) (Santa Cruz), p73 (1:100) (Abcam) or Ki67 (1:20) (Invitrogen) at 4° C. Secondary antibodies tagged with fluorophore were then added for one hour, followed by DAPI counter-staining for 30 minutes.

***In situ* hybridization**

In situ hybridization was performed on 30-µm sections as described previously(*47*) utilizing a probe against ColXa1 (a gift from Prof. Bjorn Olsen, Harvard Medical School) labelled with digoxigenin (DIG) in accordance with the manufacturer's instructions (Roche Inc.). Samples were then treated with either Fab fragments of anti-DIG antibody (Sigma) and NTM (Sigma) for colorimetric visualization or with anti-DIG antibody labelled with HRP (Sigma) and the TSA kit (Perkin Elmer) for fluorescent visualization.

Atomic Force Microscopy

120-150-µm thick sections of live rat tibia bones were obtained by vibratome (Thermo Fisher Scientific) and mounted onto glass discs using silicone grease from the Bruker fluid cell accessory kit (Bruker, USA). The force spectroscopy measurements were performed using a MultiMode 8 atomic force microscope with a Nanoscope V controller and E scanner (Bruker). The cell-containing regions of interest for acquisition of the force-distance curves were selected under the optical microscope in combination with the AFM instrument.

The force-distance curves were acquired employing CP-PNP-BSG colloidal probes (NanoandMore GmbH, Germany) with a 5-µm borosilicate glass microsphere attached to the 200-µm cantilever. The spring constants of the cantilevers were 0.06-0.09 N/m (as determined by the thermal tune procedure).

All measurements were conducted at 25^0 C and all tissue was handled in DMEM/F12 medium containing HEPES on ice. At least 70 individual force-distance curves were acquired for each type of cell by ramping over the surface and a total of 30 cells from 3 different animals were examined. These force-distance curves were processed with the NanoScope Analysis v.1.10 software (Bruker). Utilizing retract curves, the elastic modulus E was extracted from these force-distance curves by fitting according to the Hertzian model of contact mechanics.

Nanoindentation

The local mechanical characteristics of cartilage samples from 10-day-old rat and 30-day-old mice were assessed with a Piuma Nanoindenter (Optics11, Netherlands) adapted for soft materials. These measurements were performed on 220-250-µm sections of alive tissue (without fixation and freezing) obtained by vibratome (Thermo Fisher Scientific) at 2-4 ^{o}C. Thereafter, the sections were stained with PI (Sigma) and CalceinAM (Sigma) to confirm cell viability.

The nanoindenter has a controller, an optical fiber and a spherical tip for acquisition of the force-displacement curves. The tip is attached to a flexible cantilever, the displacement of which following contact with a surface is measured by an interferometer via an optical fiber.

To obtain the Young's modulus, the probe was immersed 5 μm into each sample at each point of measurement and modulus for each point was computed according to the Hertzian contact mechanics model of a spherical body indenting a flat surface, using the built-in Piuma software.

To study the mechanical characteristics of the cartilage of 10-day-old rat and 30-day-old mice, we used a cantilever with a spring constant of 4.14 N/m and a tip with a 45.5-μm radius of curvature. These measurements were conducted in phosphate buffered saline (PBS) cooled to 2-4 °C to maintain cell viability with the samples immobilized with a specially designed holder. During measurement the probe was always immersed deeply enough in the fluid to avoid errors due to adhesion forces at the air-water interface. To determine the Young's modulus a 1350×400 μm area of the rat samples was mapped in steps of 45 μm along the X-axis and 100 μm along the Y-axis. For mice, this area of mapping was 585×360 μm, with steps of 45 μm along both axes. The effective Young's modulus was computed, its distribution over the surface plotted, and the mean ± standard deviation (SD) calculated.

Finite Element Analysis

The effects of an SOC on the distribution of stress in the zones of bone growth were explored by numerical simulations. Following reasoning described previously(*27*), a plane-strain 2D domain was considered, in order to simplify the complex geometry of the end of the bone, and thereby clarify fundamental aspects of the response. The model thus took five sub-domains into consideration. The geometry of this simulation domain was a slight modification of (*27*), with a total height of 66 mm, radius at the top of 17 mm, and bottom width of 25 mm. The cortical bone was given a width of 2.5 mm (measured horizontally). The thickness normal to the 2D plane was by definition 1 mm. Only the top part of the model is shown in results figures.

The main parameter in these simulations was the presence or absence of an SOC or other stiffer tissues, introduced by providing this domain with a stiffness at least equal to that of the cartilage domain. Non-linear strains were taken into consideration, but the materials in all subdomains were considered to be linearly elastic, as described by a Young's modulus E_i and a Poisson ratio ν_i. We used the same material properties as (*27*), and in particular for cartilage E_C= 6 MPa, ν_C= 0.47. When included, the SOC was defined in a subdomain with E_D= 500 MPa, ν_D= 0.20. Thus, the stiff tissue had the material properties of dense cancellous bone, i.e., approximately 80-fold stiffness compared to cartilage.

In all cases, the bottom edge of the complete model had zero displacement vertically, and the outside edges of the cortical bone zero displacement horizontally. Applied to different 45° sectors of the semi-circular top, the pressure was modelled as maximal on the center of the given sector (300 kPa for physiological level, 3MPa for supra-physiological), falling quadratically and symmetrically to zero on the two neighboring sector borders. In light of the symmetry of the domain, only the top or right-hand side

was loaded (except for a verification case to (*27*), not shown). The direction and integrated total force of loading were affected slightly by the finite deformation of the domain.

Different components or comparison values of stress (measured as the second Piola-Kirchhoff stress relative to the unstressed reference volume) were evaluated. Primary focus was on the hydrostatic stress, the lowest principal stress (always compressive), and the octahedral shear stress, providing different perspectives on the response to external loading. Since the situations considered were dominated by compressive stresses, the signs for the two first have been changed in figures. Stress values are plotted on the deformed shape of the domain, without magnification of the deformation.

Numerical simulations of the response to loading were based on parameterized finite element approximations, and performed in the Comsol Multiphysics software (version 5.2, Comsol AB, Stockholm, Sweden.)

With similar loads, this model resulted in a stress distribution in and deformation of the cartilaginous epiphysis closely similar to those reported by (*27*).

Model design for stem tetrapods and archosaurs were based on (*2, 3*) and (*9, 10*) respectively.

Quantitative PCR

Proximal end growth plate of mouse and rat tibia was dissected and homogenized in liquid nitrogen for subsequent RNA extraction by Trizol and RNA purification by the RNeasy kit (Qiagen). Only RNA samples with an A260/A280 value between 1.8 and 2.0 were used. Extracted RNA was reverse transcribed into cDNA using a kit from Takara. qPCR was performed using the SYBR Green I supermix (BioRad) and analyzed using the ΔCt method by normalizing with the house keeping gene GAPDH. Three growth plates from independent animals were analyzed for each condition.

Statistical analysis

The values presented as means ± standard deviations of at least three independent experiments. The unpaired Student's t-test and one way ANOVA were utilized to calculate P-values if not otherwise indicated.

Figures

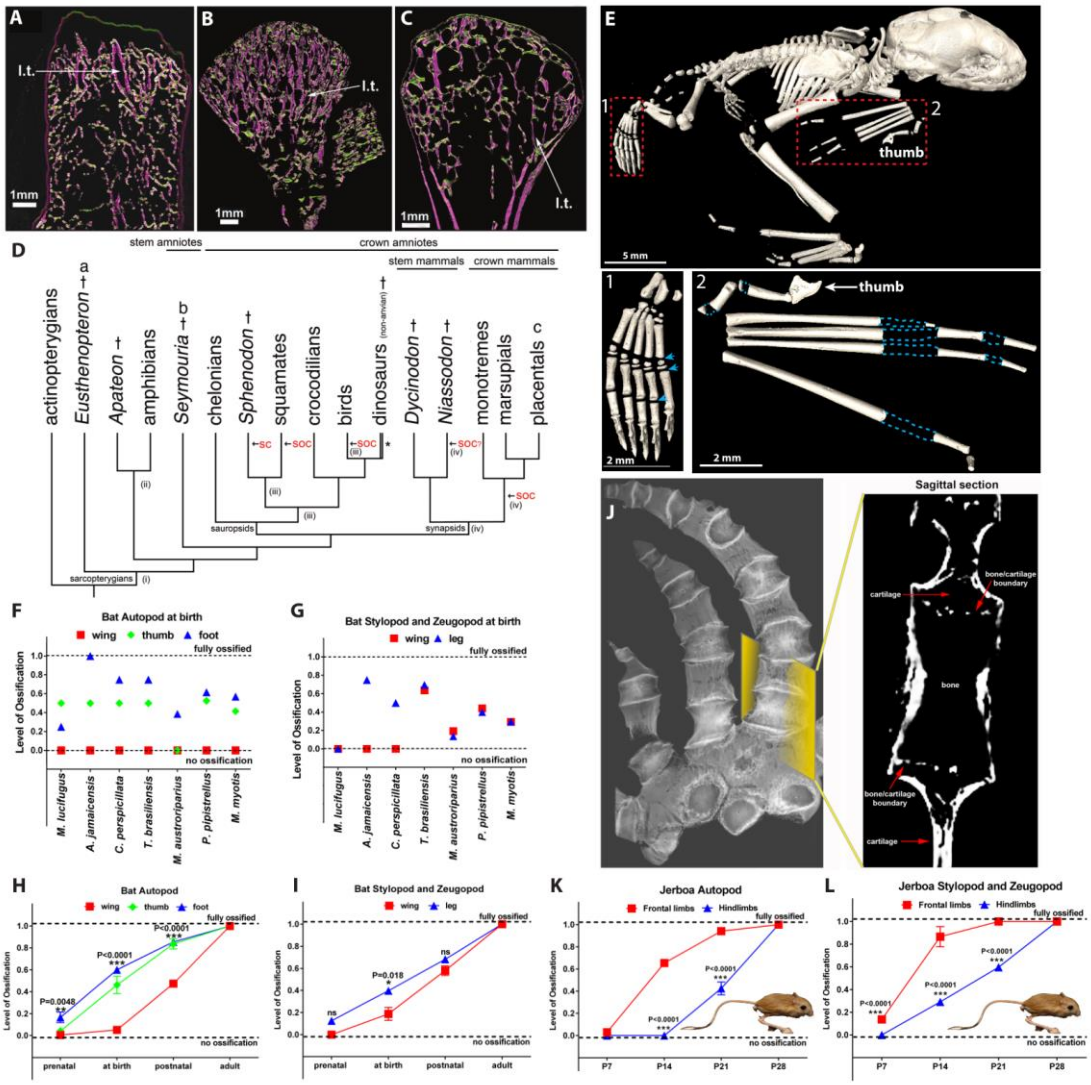

Fig. 1 Evolutionary appearance of the SOC and its correlation with the mechanical demands.

(**A** to **C**) The proximal humeral metaphyses of Eusthenopteron (A), Seymouria (B) and Sciurus vulgaris (red squirrel) (C). The longitudinal trabeculae resulting from endochondral ossification at the base of the growth plate in adults are shown in pink, while the transverse trabeculae appear green. The longitudinal trabeculae (l.t.) are projections of marrow invading the growth plate. (**D**) The phylogeny of osteichthyans, illustrating the major changes in the evolution of the epiphyses of long bones. The black arrows indicate the presence of a secondary center (SC) or a secondary ossification center (SOC). (i) Estimated appearance of endochondral formation of long bones, based on the fossil record to date; (ii) Cartilaginous epiphyses in long-bones; (iii) Hypothetical presence of an ancestral SC in sauropsids; (iv) Hypothetical presence of an ancestral SOC in synapsids. * indicates paraphyly within the group. (**E**) microCT image of a 1-3-day-old Pipistrellus pipistrellus bat. (1) foot, with arrows pointing to growth plates, (2) wing, with dashed blue lines outlining the areas of non-ossified cartilage. (**F** and **G**) Ossification of the autopod (F) and of the stylopod and zeugopod (G) in 7 bat species at birth. (**H** and **I**) Generalized pattern of ossification of the autopod (H) and stylopod and zeugopod (I) of 6 bat species combined (Myotis lucifugus, Artibeus jamaicensis, Carollia perspicillata, Tadarida

brasiliensis, Myotis austroriparius and Myotis myotis). (**J**) CT image of an adult killer whale Orcinus orca and a virtual sagittal section of the metacarpal II demonstrating the absence of the SOC. (**K** and **L**) Ossification of the autopod (K) and stylopod and zeugopod (L) of *Jaculus jaculus* (three-toed jerboa) at various postnatal stages. Data are means ± SD representing inter-individual variation, One-way ANOVA. In (K) and (L), n=2 jerboa analyzed. ns, not significant.

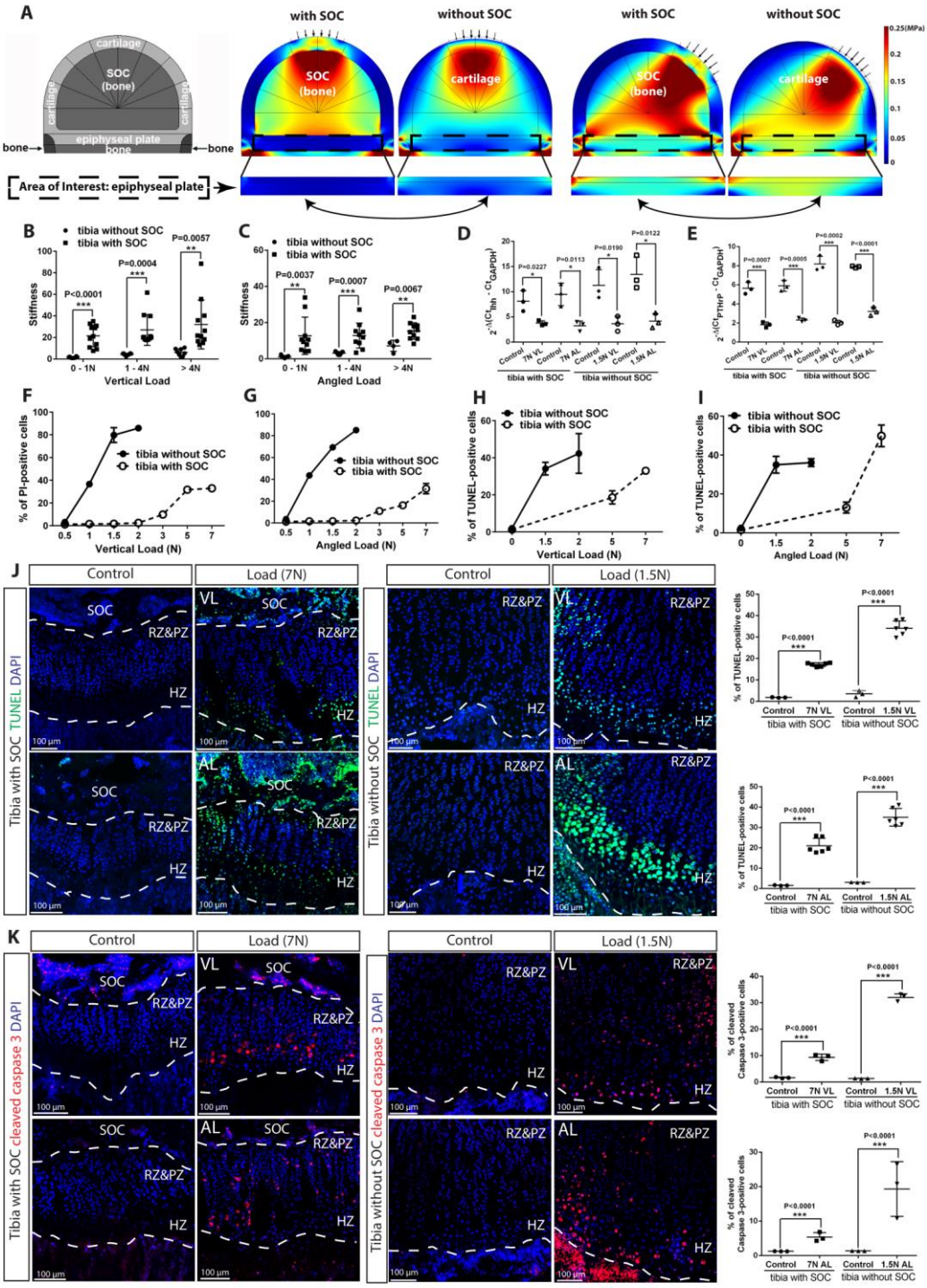

Fig. 2 The SOC protects epiphyseal chondrocytes from apoptosis induced by mechanical stress.

(**A**) Octahedral stress from FEA modeling with a physiological load. The small arrows indicate the direction of loading. The two-headed curved arrows indicate areas for comparison. (**B** and **C**) The stiffness of bones with fully developed SOCs (tibia with SOC) and with immature SOCs (tibia without SOC) was measured at different loads and in both the vertical (B) and angled (C) directions. (**D** and **E**) QPCR analysis of Indian hedgehog (Ihh) (D) and parathyroid hormone related peptide (PTHrP) (E) in the epiphyseal end of tibia with and without SOCs. (**F** to **I**) Quantification of propidium iodide- (PI) (F and G) and TUNEL- (H and I) positive cells in the growth plates of tibia with and without SOCs loaded vertically (F, H) or at an angle (G, I). (**J** and **K**) Representative images and quantification of TUNEL staining (green) (J) and cleaved Caspase 3 staining (red) (K) in the growth plates of loaded tibias with and without SOCs. DAPI was used for counterstaining (blue). Data are means ± SD, two-tailed Student's t test. In (B), n=10 for "tibia with SOC" at all loads; n=9 for "tibia without SOC" at 0–1N and 1-4N, n=4 for >4N. In (C), n=11 for "tibia with SOC" at all loads; n=8 for "tibia without SOC" at all loads. In (D) to (K), n=3. The control and loaded tibia were from the same animal. VL, vertical load, AL, angled load. RZ&PZ, resting zone & proliferative zone combined, HZ, hypertrophic zone. "tibia with SOC" and "tibia without SOC" in the figure refer to tibias from 30-day-old mice and 10-day-old rats, respectively (see Fig. S5, B, C).

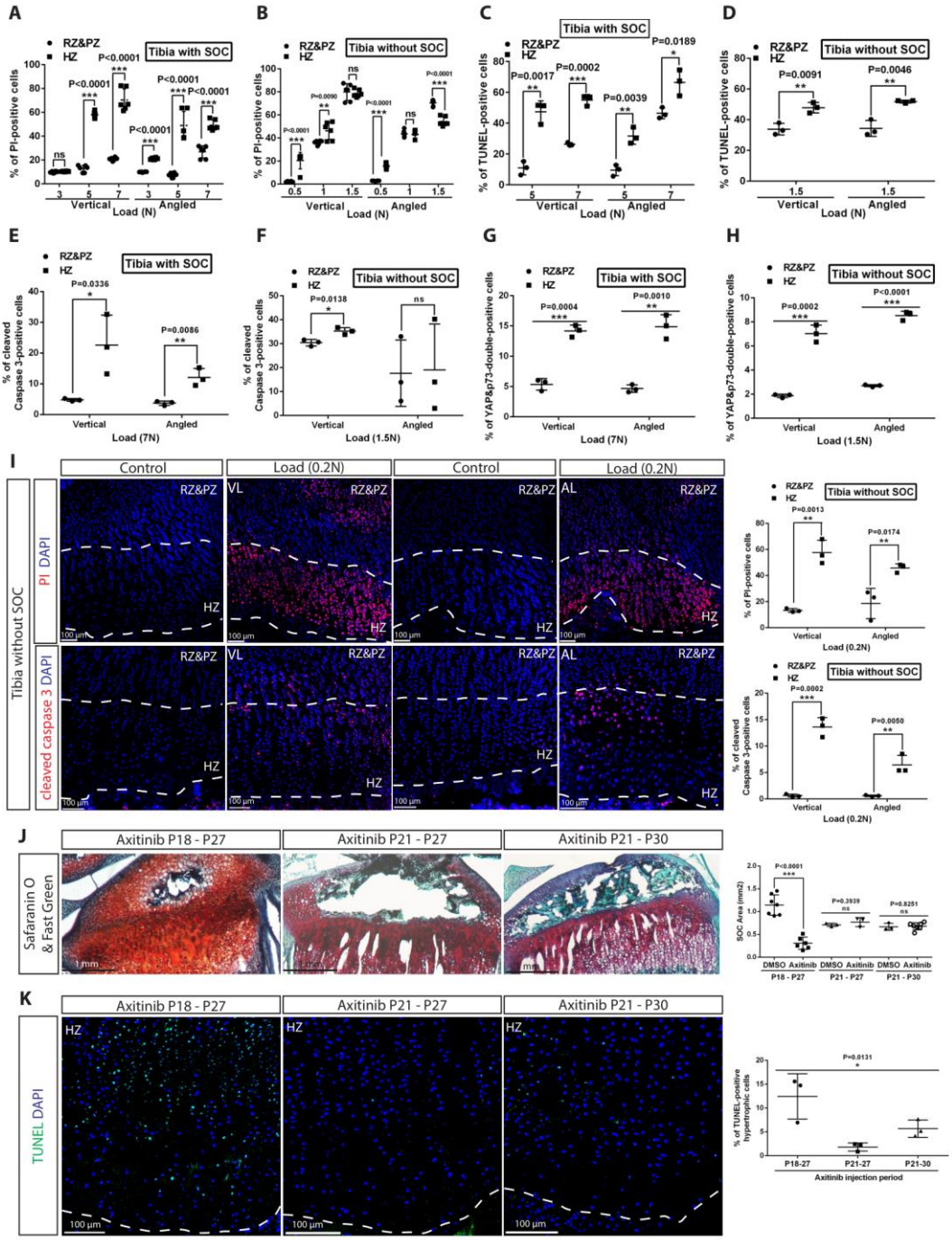

Fig. 3 Hypertrophic cells are most sensitive to mechanical stress.

(**A** to **D**) Comparison of the extent of cell death in the resting+proliferative zones (RZ&PZ) and hypertrophic zone (HZ) of the vertically and angularly loaded growth plates with (A and C) and without (B and D) SOCs as assessed by PI staining (A and B) and TUNEL analysis (C and D). (**E** to **H**) Distribution of immunohistological staining along longitudinal axis for cleaved Caspase-3 (E to F) and YAP+p73 (G to H) in vertically and angularly loaded tibia with (E and G) and without (F and H) SOCs. (**I**) Representative images and quantification of propidium iodide (PI) staining (upper panel) and cleaved Caspase 3 staining (lower panel) in the growth plates of vertically or angularly 0.2N loaded tibias without SOCs. The control and loaded tibia were from the same animal. (**J**) Representative histology images of the tibia epiphysis and quantification of the SOC size of wild type mice injected with axitinib at various time periods. P refers to postnatal day. (**K**) Representative images and quantification of TUNEL staining

(green) in the hypertrophic cells of the tibia growth plate of the mice injected with axitinib. DAPI was used for counterstaining (blue) in I and K. Data are means ± SD, two-tailed Student's t test. In (A) to (K), n=3. ns, not significant. "tibia with SOC" and "tibia without SOC" refer to tibias from 30-day-old mice and 10-day-old rats, respectively (see Fig. S5, B, C).

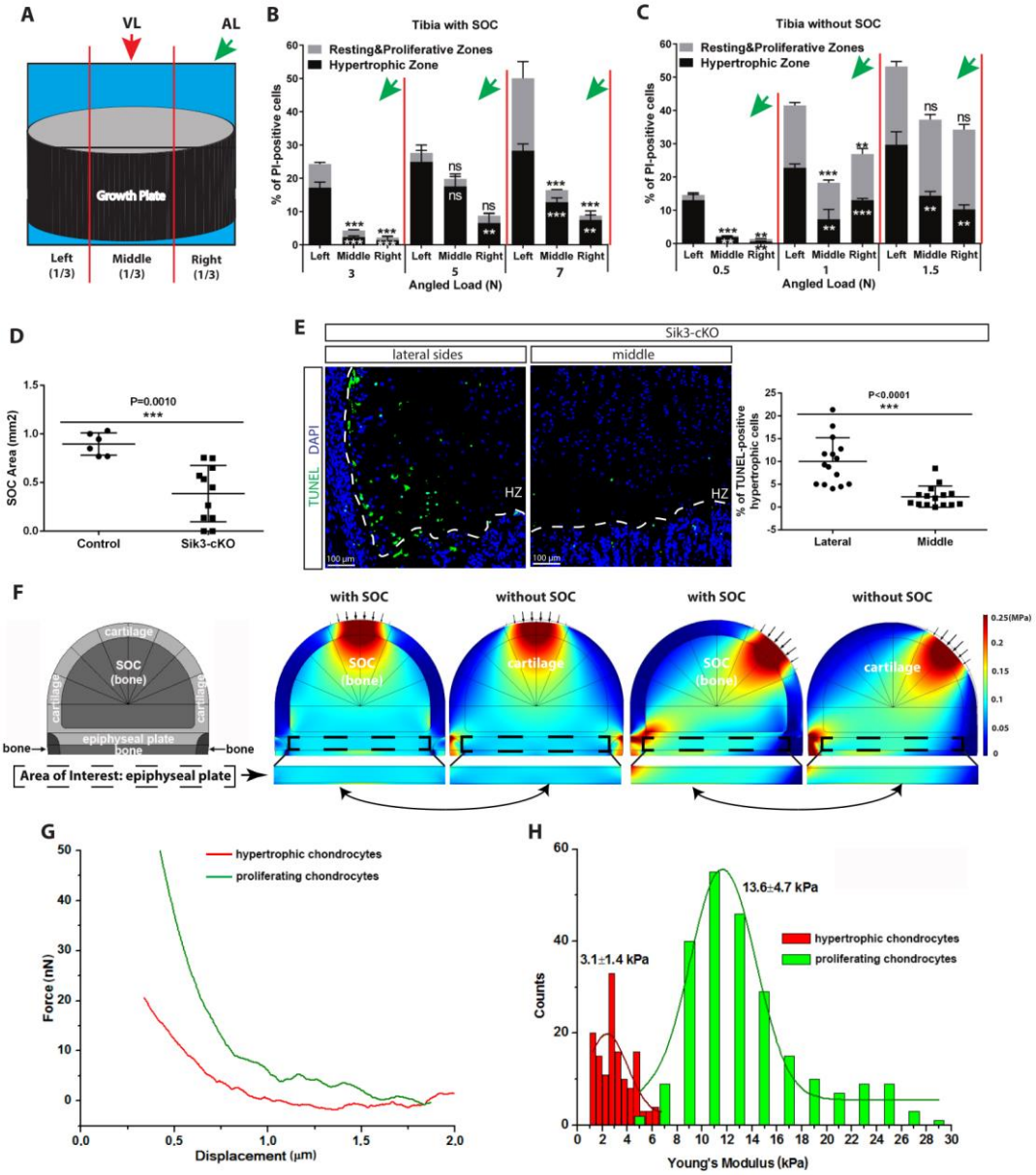

Fig. 4 The low stiffness of hypertrophic chondrocytes renders them sensitive to mechanical stress.

(**A**) Schematic illustration of a section plan and loading directions in relation to the quantitative analysis of cell death distribution in the lateral-medial direction presented in (B and C). The growth plate is divided into three equal parts, (left, middle and right) in relationship to the angle at which the load was applied (green or red arrows). (**B** and **C**) Quantification of propidium iodide (PI)-positive chondrocytes in the resting&proliferative zones and hypertrophic zone of tibias with (B) and without (C) SOCs subjected to an angled load (AL, green arrow, always applied from the right). Data are means ± SD, One-way ANOVA. **, P<0.001 and ***, P<0.0001 in comparison with the left portion. ns, not significant. The black and white asterisks

indicate the significance for the resting&proliferative and hypertrophic zones, respectively. (**D**) Quantification of the SOC size of postnatal day 28 Sik3-FL/FL (Control) and Col2-Cre:Sik3-FL/FL (Sik3-cKO) mice. (**E**) Representative images and quantification of TUNEL staining (green) between the lateral and middle parts of Sik3-cKO mice. DAPI was used for counterstaining (blue). HZ, hypertrophic zone. In (D) and (E), data are means ± SD, two-tailed Student's t test, n=3 for "Control" and n=5 for "Sik3-cKO". (**F**) Principal compressive stress from FEA modeling with physiological loading level. The small arrows indicate the direction of loading. The two-headed curved arrows indicate areas for comparison. (**G**) Typical force curves for hypertrophic and proliferating chondrocytes obtained by atomic force microscopy. (H) Comparison of the elastic moduli of hypertrophic and proliferating chondrocytes.

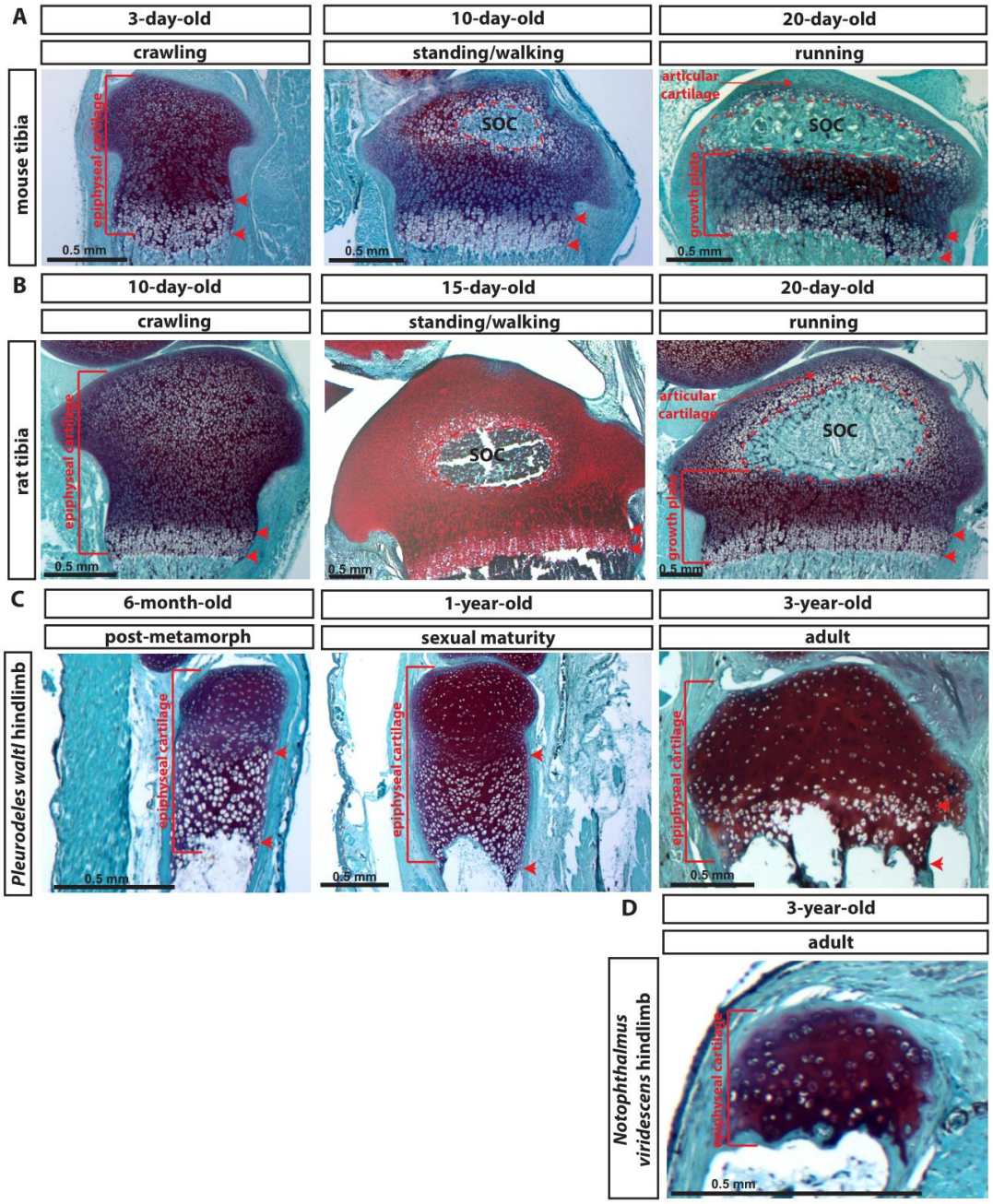

Fig. S1 Development of articular and epiphyseal cartilage in rodents and salamanders.

(**A** to **D**) Representative safranin O and fast green staining of sections of the epiphyseal end of the tibia of mouse (A), rat (B), and the hind limb of salamander species Pleurodeles waltl (C) and Notophthalmus viridescens (D). The dashed red lines outline the SOC. Red arrow heads mark the zone of hypertrophic cells. Walking behavior was assessed by daily observation. Pleurodeles waltl is a Spanish newt that spends most its life in water. Notophthalmus viridescens is an American newt that is aquatic as juvenile and terrestrial when adult.

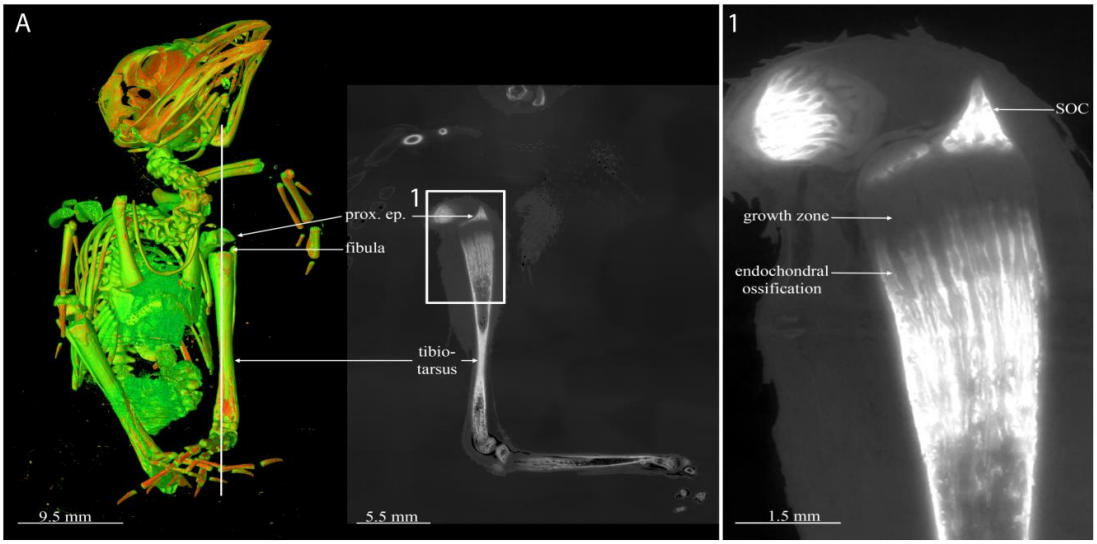

Fig. S2 (A) A synchrotron scan of a juvenile sparrow demonstrates the presence of an SOC. 1, a virtual thin section of the proximal epiphysis. prox. ep., proximal epiphysis.

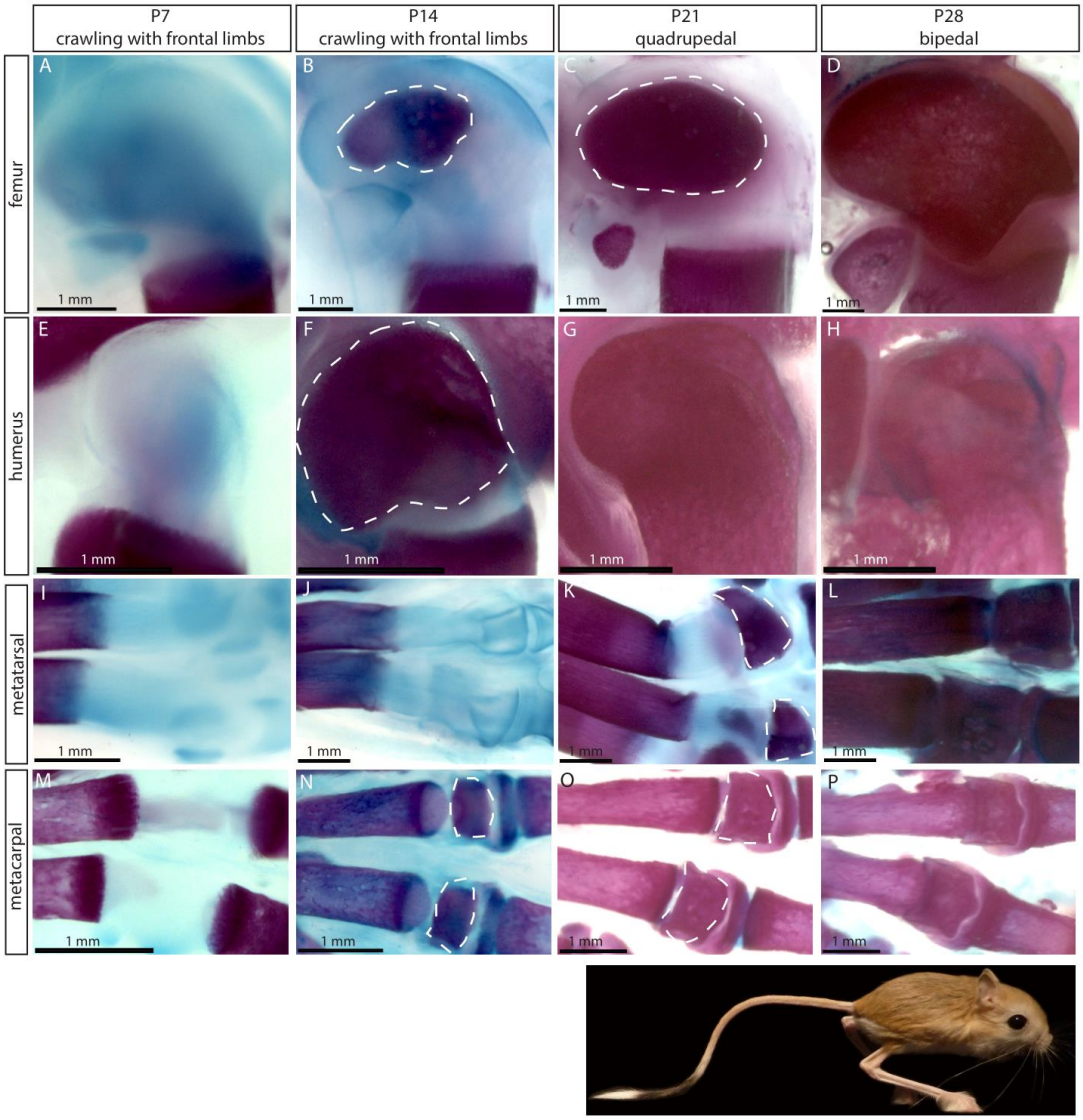

Fig. S3 (**A** to **P**) Alcian blue and alizarin red staining of femur (A to D), humerus (E to H), metatarsal (I to L) and metacarpal (M to P) of *Jaculus jaculus* (three-toed jerboa) at various postnatal (P) time points. The dashed white lines outline the SOC. The gait pattern was assessed by weekly observation (see Video S2).

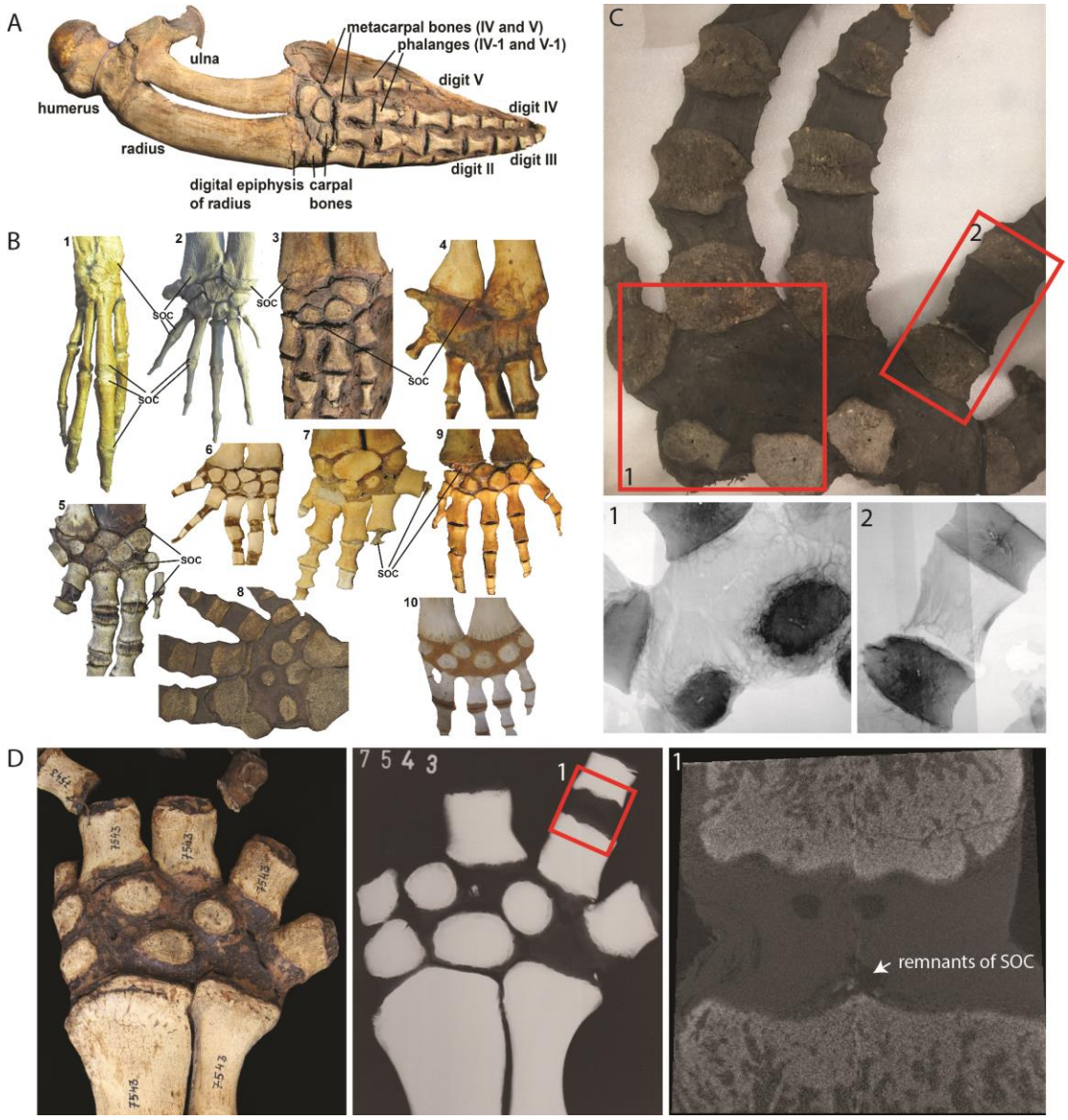

Fig. S4 (**A**) Forelimb bones of the minke whale Balaenoptera acutorostrata. (**B**) Comparative anatomy of the bony and cartilaginous epiphyses in the distal portion of the forelimbs of various cetacean whales. (B1) *Maiacetus inuus*, (B2) *Dorudon atrox*, (B3) minke whale *Balaenoptera acutorostrata*, (B4) North Atlantic right whale *Eubalaena glacialis*, (B5) pilot whale *Globicephala melas*, (B6) boto river dolphin *Inia geoffrensis*, (B7) narwhal *Monodon monoceros*, (B8) killer whale *Orcinus orca*, (B9) juvenile and (B10) subadult sperm whale *Physeter catodon*. (**C**) Sample X-ray image of an adult killer whale *Orcinus orca* (same species as B8) with the highlighted areas (1, 2) in the corresponding image on the left. (**D**) Sample (left) and X-ray (right) images of an adult beluga whale *Delphinapterus leucas*. (D1) Micro-CT reconstruction of the highlighted phalange joint.

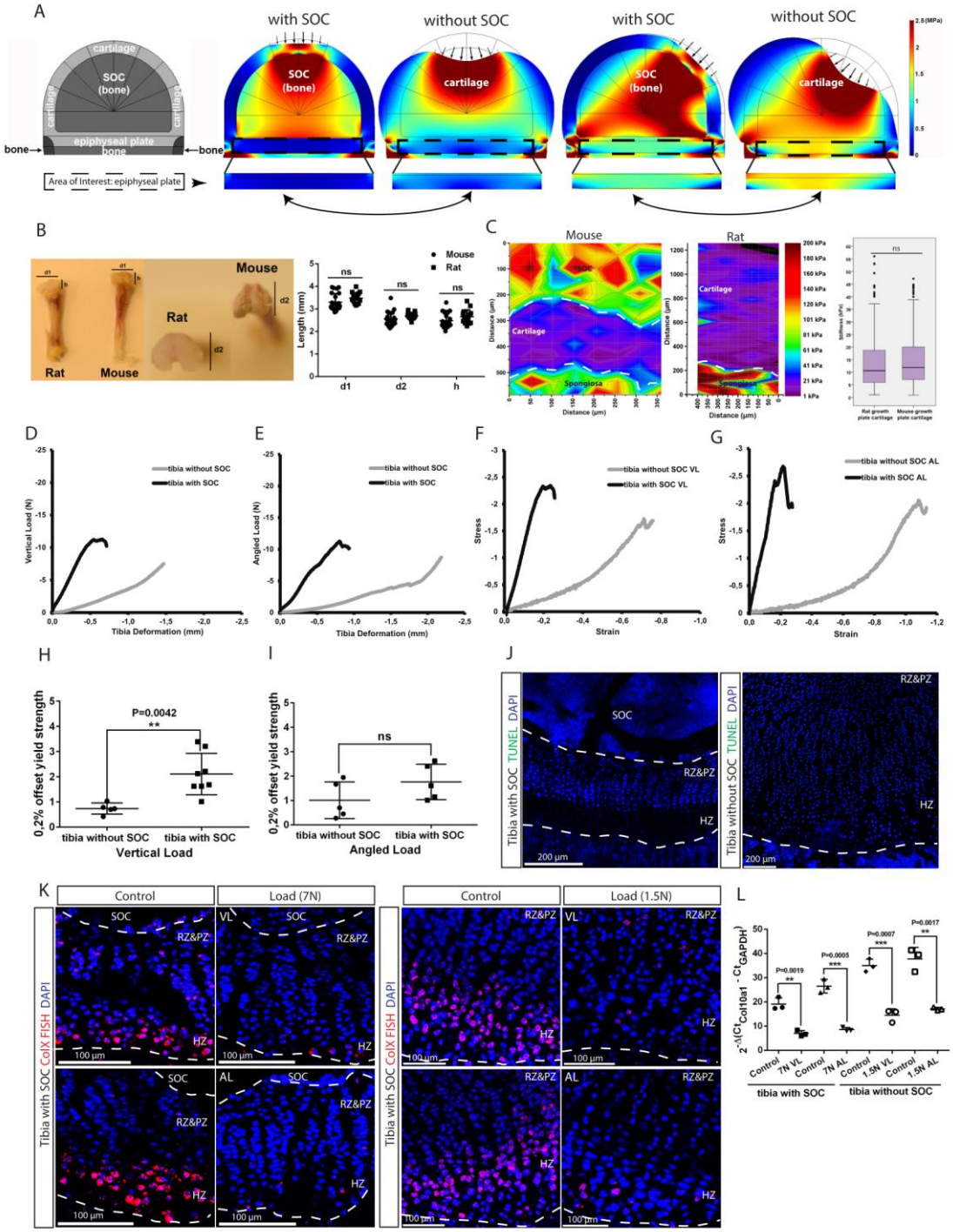

Fig. S5 (**A**) Octahedral stresses from FEA modeling with supra-physiological loading (3 MPa). The small arrows indicate the direction of loading and the two-headed curved arrows indicate areas for comparison. (**B**) The epiphysis of mouse (30-day-old) and rat (10-day-old) tibia with and without an SOC, have similar physical dimensions (d1, d2, h). (**C**) Representative images and quantification of the nanoindentation test of 30-day-old mice and 10-day-old rats. (**D** to **G**) Representative load/deformation (D and E) and stress/strain (F and G) curves of vertically (VL) (D and F) and angularly (AL) (E and G) loaded tibias with and without SOCs. (**H** and **I**) Elasticity of tibias with and without SOCs under vertical (H) and angled load (I). (**J**) Representative images of growth plates

of tibias with and without SOCs fixed after dissection and prior to loading. TUNEL staining (green) and counterstaining of the nucleus with DAPI (blue). (**K**) Fluorescent *in situ* hybridization of Collagen type X (ColX) in the loaded growth plates of tibias with and without SOCs. VL, vertical load, AL, angled load. RZ&PZ, resting zone & proliferative zones, HZ, hypertrophic zone. (**L**) QPCR analysis of ColX level in the epiphyseal end of tibia with and without SOCs exposed to different loading. Data are means ± SD, two-tailed Student's t test, except in (C) where Mann-Whitney U test was used. In (B), n=23 for "Mouse" and n=15 for "Rat". In (C), n=5 for "Mouse" and n=4 for "Rat". In (H), (I) and (L), n=3. ns, not significant.

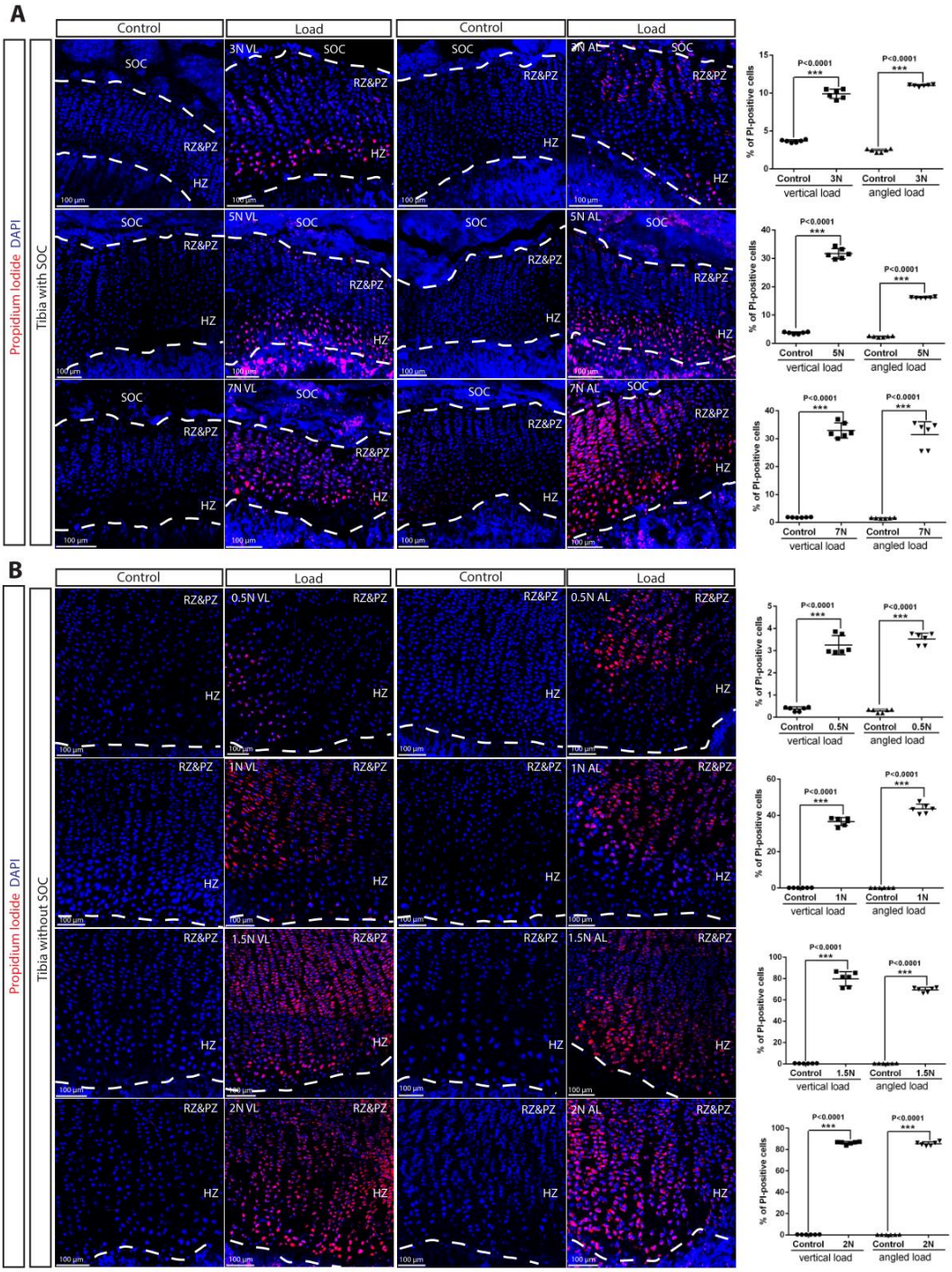

Fig. S6 (**A** and **B**) Representative images and quantification of the distribution of propidium iodide (PI)-positive cells in the growth plates of tibia with (A) and without a SOC (B) loaded vertically or angularly. RZ&PZ, resting zone & proliferative zones, HZ, hypertrophic zone. "tibia with SOC" and "tibia without SOC" refer to tibias from 30-day-old mice and 10-day-old rats respectively (see Fig. S5, B, C). Data are means ± SD, two-tailed Student's t test. In (A) and (B), n=3.

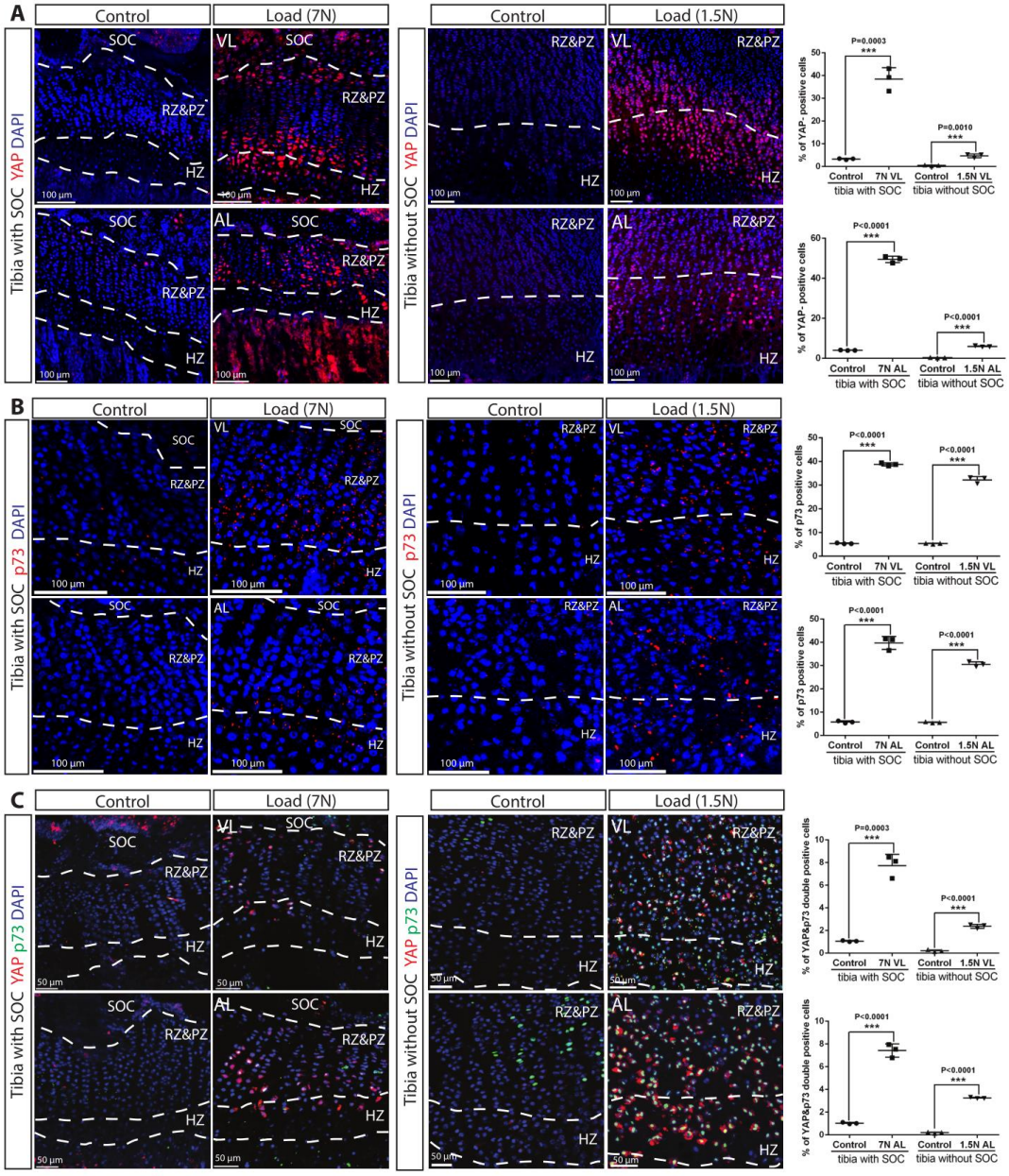

Fig. S7 (**A** to **C**) Immunostaining and quantification of YAP (A), p73 (B) and YAP + p73 double-positive cells (C) in the growth plates of loaded tibias with and without SOCs loaded vertically (VL) and angularly (AL). RZ&HZ, resting zone & proliferative zone, HZ, hypertrophic zone. "tibia with SOC" and "tibia without SOC" refer to tibias from 30-day-old mice and 10-day-old rats respectively (see Fig. S5, B, C). Data are means ± SD, two-tailed Student's t test. In (A) to (C), n=3.

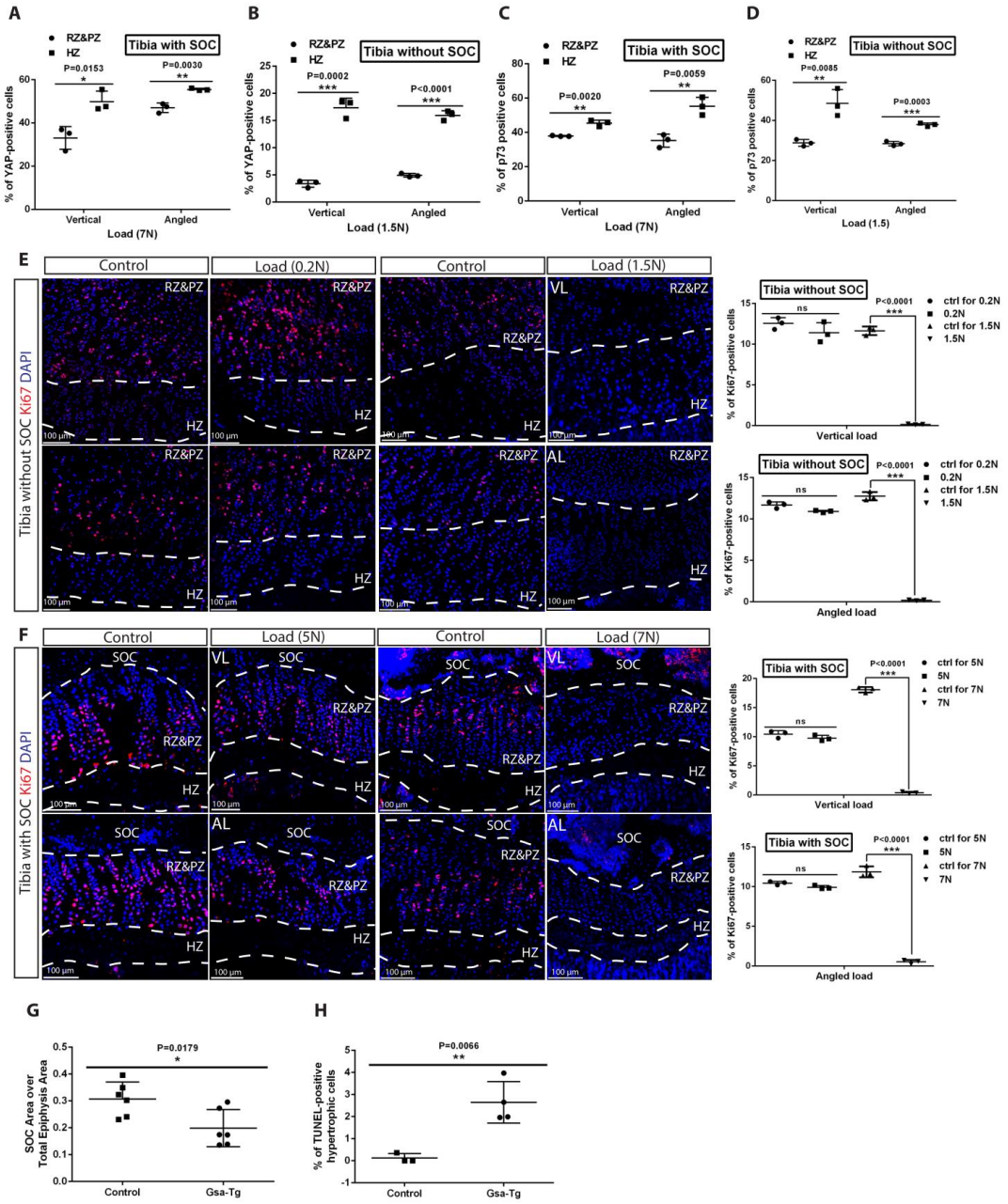

Fig. S8 (**A** to **D**) Comparison of YAP (A and B) and p73 (C and D) staining between the resting plus proliferative zones (RZ&PZ) and hypertrophic zone (HZ) in the growth plates of tibias with (A and C) and without (B and D) SOCs. (**E** and **F**) Representative images and quantification of the ki67 staining in the growth plates of tibias with (F) and without (E) SOCs. (**G** and **H**) Quantification of SOC size (G) and TUNEL staining (H) of the hypertrophic cells in the growth plates of $_{stop}Gs\alpha^{R201H}$ (Control) and Prx-Cre:$Gs\alpha^{R201H}$ (Gsα-Tg) mice. Data are means ± SD, two-tailed Student's t test. In (A) to (H), n=3. ns, not significant.

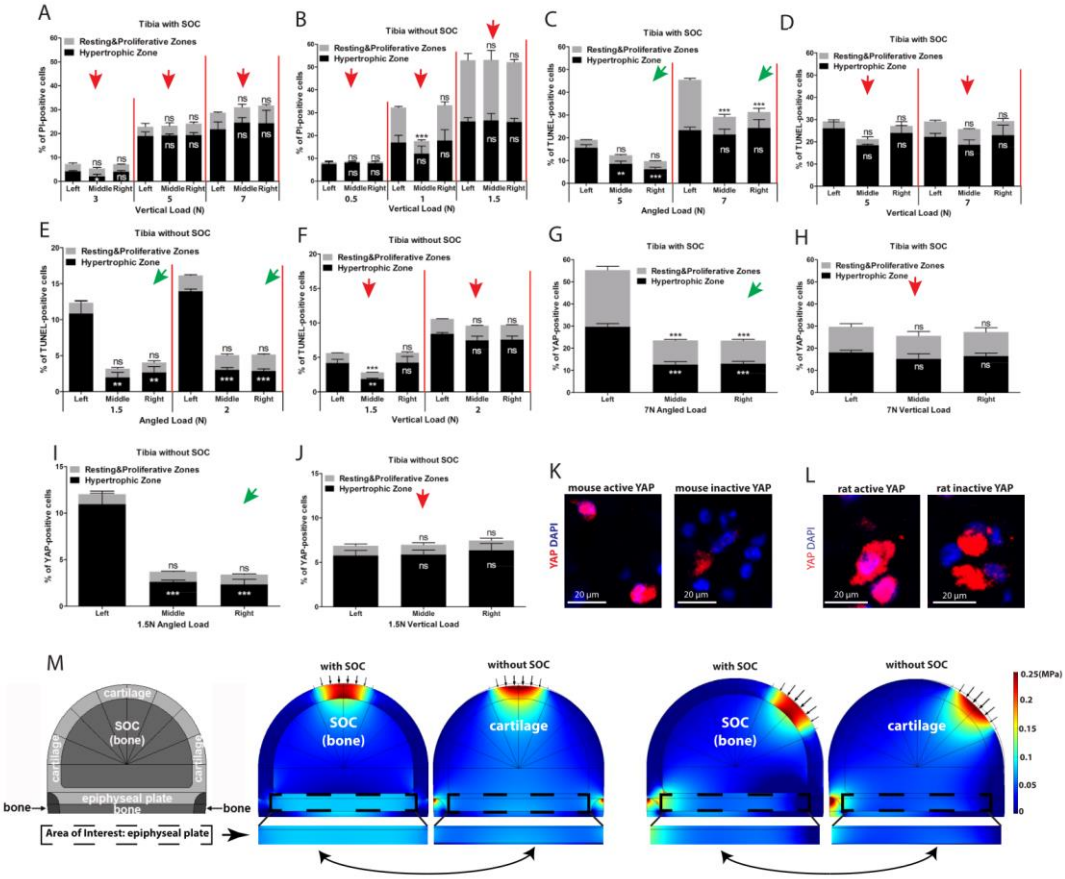

Fig. S9 (**A** and **B**) Quantification of PI-positive chondrocytes in the lateral-medial direction of the growth plate of tibia loaded vertically with (A) and without (B) an SOC (see Fig. 4A for details). (**C** to **F**) Quantification of TUNEL-positive chondrocytes in the lateral-medial direction of the growth plate of tibia with (C and D) and without (E and F) an SOC and subjected to angular (C, E) or vertical (D, F) loading. (**G** to **J**) Quantification of the distribution of YAP-positive chondrocytes in the lateral-medial direction within the resting&proliferative and hypertrophic zones of the growth plate of angularly (G, I) and vertically (H, J) loaded tibia with (G and H) and without (I and J) an SOC. Only active YAP in the nucleus (as demonstrated in k-l) was quantified. The red and green arrows indicate the direction of loading (see the legend to Fig. 4a for more details). Data are means ± SD, One-way ANOVA. **, P<0.001 and ***, P<0.0001. In (A) to (J), n=3. ns, not significant.The black and white asterisks indicate p-values for the resting&proliferative and hypertrophic zones, respectively. (**K** and **L**) Immunostaining of active (nuclear) and inactive YAP in mouse (K) and rat (L) chondrocytes. (**M**) Hydrostatic compressive stress on epiphyseal plates from FEA modelling with physiological loading level. The small arrows indicate the direction of loading and the two-headed curved arrows indicate areas for comparison.

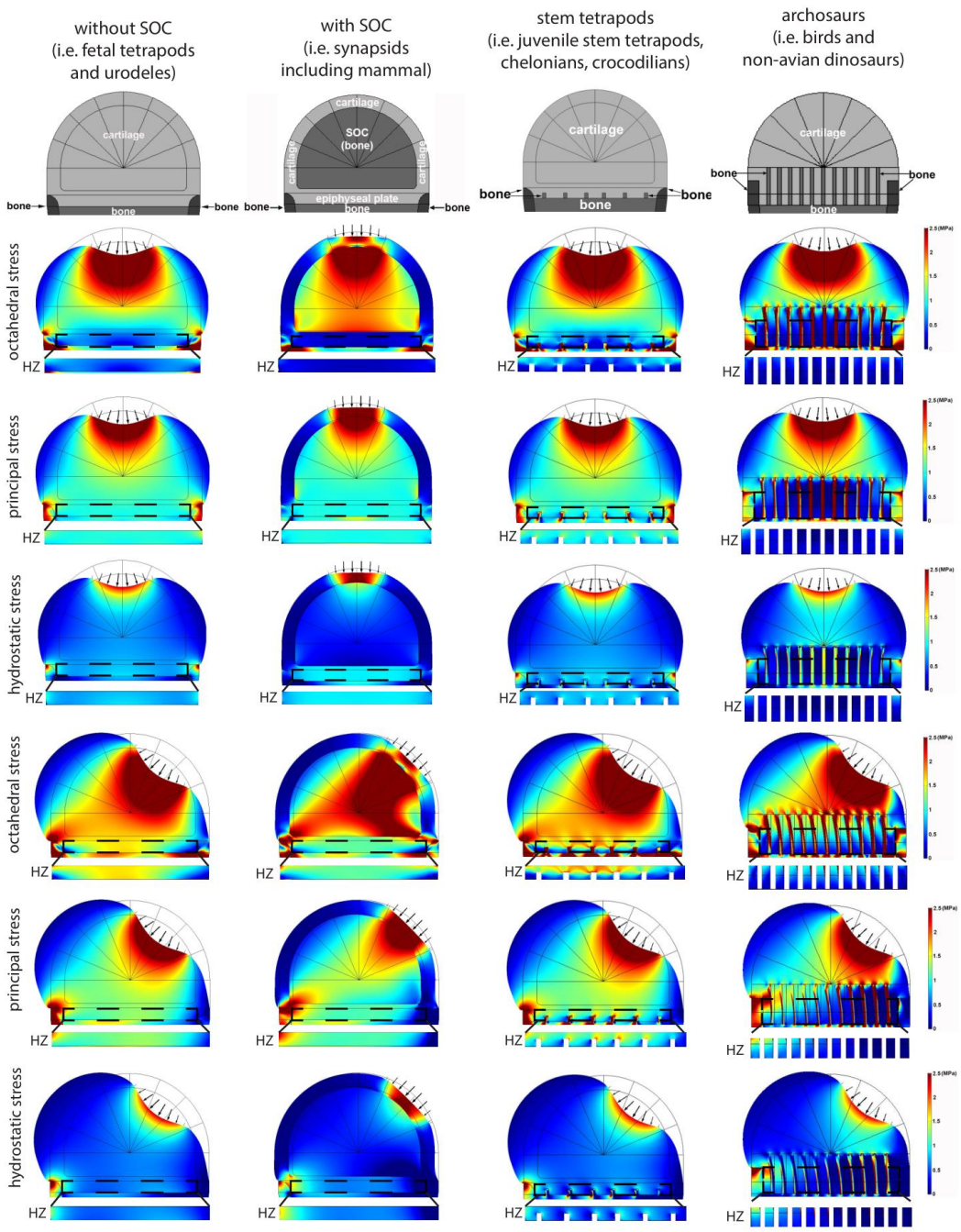

Fig. S10 Deformation and distribution of comparison stresses from FEA simulation in different evolutionary taxa. The columns refer (from left to right) to "without SOC" (i.e., fetal tetrapods and urodeles), "with SOC" (i.e., synapsids, including mammal), "stem tetrapods" (i.e., juvenile stem tetrapods, chelonians, crocodilians) and archosaurs (i.e., birds and non-avian dinosaurs). For comparison of structural functionality, the same basic geometry and materials were utilized in all cases. The small arrows indicate the direction of loading. Supra-physiological loading (3 MPa) was modeled. The illustrations of octahedral stress without and with a SOC are identical to those in Fig. S2, A and are presented here to allow direct comparison. The hypertrophic zone free of bony elements is presented under each model for direct comparison. Hypertrophic zone, HZ.

Video S1 3D model based on microCT surface images of a 1-3-day-old Pipistrellus pipistrellus s.l. (common pipistrelle bat). The age could not be determined more precisely.

Video S2 CT scan of the manus of a killer whale Orcinus orca.

Video S3 Development of gait in Jerboa.

Supplementary data file S1 Primary data on the level of ossification of the individual bones of all species of Chiroptera analyzed.

Author Contributions

A.S.C. designed the study. M.X. conceived the study under the guidance of A.S.C. M.X. performed all of the experiments except those specified below. P.G. performed the studies on SOC evolution in cetaceans. K. G. helped with X-ray scans with the Beluga whale. A.N.H., B.M., K.F. and I.A. analyzed SOC development in chiroptera. J.E., P.T. and S.S. modeled the synchrotron scan data and examined SOC evolution in early tetrapods, amphibians and stem amniotes. L.L., P.N. and M.C. assisted with the biological experiments. M.K. and A.S. assisted with the experiments on rat and salamander, respectively. I.L.A. and C.G. helped with application of the load testing instrument. P.T., E.V.M., S.K., B.S. and A.A. performed the atomic force microscopy and nanonindentation analysis. L.T.S. and M.B. performed experiments on Prx-Cre:Gsα^{R201H} mice. S.N. and H.M.K. contributed to experiments with SIK3 cKO mice. A.S. and K.C. contributed jerboa experimental data. A.E. developed the finite element analysis. M.X. and A.S.C. wrote the paper with the help of I.A, S.S. P.G and A.N.H. All authors critically reviewed this manuscript and approved the final draft.

References

1. L. Yang, K. Y. Tsang, H. C. Tang, D. Chan, K. S. Cheah, Hypertrophic chondrocytes can become osteoblasts and osteocytes in endochondral bone formation. *Proceedings of the National Academy of Sciences of the United States of America* **111**, 12097-12102 (2014); published online EpubAug 19 (10.1073/pnas.1302703111).
2. S. Sanchez, P. Tafforeau, P. E. Ahlberg, The humerus of Eusthenopteron: a puzzling organization presaging the establishment of tetrapod limb bone marrow. *Proc Biol Sci* **281**, 20140299 (2014); published online EpubMay 07 (10.1098/rspb.2014.0299).
3. S. Sanchez, P. Tafforeau, J. A. Clack, P. E. Ahlberg, Life history of the stem tetrapod Acanthostega revealed by synchrotron microtomography. *Nature* **537**, 408-411 (2016); published online EpubSep 15 (10.1038/nature19354).
4. B. K. Hall, *Bones and Cartilage Developmental and Evolutionary Skeletal Biology*. (Elsevier Academic Press, San Diego, ed. 2, 2005).
5. L. L. Phillip T. Newton, Baoyi Zhou, Christoph Schweingruber, Maria Hovorakova, Meng Xie, Xiaoyan Sun, Lakshmi Sandhow, Artem V. Artemov, Evgeny Ivashkin, Simon Suter, Vyacheslav Dyachuk, Maha El Shahawy,

Amel Gritli-Linde, Thibault Bouderlique, Julian Petersen, Annelie Mollbrink, Joakim Lundeberg, Grigori Enikolopov, Hong Qian, Kaj Fried, Maria Kasper, Eva Hedlund, Igor Adameyko, Lars Sävendahl, Andrei S Chagin, A radical switch in clonality reveals a stem cell niche in the epiphyseal growth plate. *Nature*, (2019)https://doi.org/10.1038/s41586-019-0989-6).

6. N. B. Frobisch, N. H. Shubin, Salamander limb development: integrating genes, morphology, and fossils. *Dev Dyn* **240**, 1087-1099 (2011); published online EpubMay (10.1002/dvdy.22629).
7. R. W. Haines, The Primitive Form of Epiphysis in the Long Bones of Tetrapods. *J Anat* **72**, 323-343 (1938); published online EpubApr (
8. R. Castanhinha, R. Araujo, L. C. Junior, K. D. Angielczyk, G. G. Martins, R. M. Martins, C. Chaouiya, F. Beckmann, F. Wilde, Bringing dicynodonts back to life: paleobiology and anatomy of a new emydopoid genus from the Upper Permian of Mozambique. *PLoS One* **8**, e80974 (2013)10.1371/journal.pone.0080974).
9. A. Chinsamy, F. Abdala, Palaeobiological implications of the bone microstructure of South American traversodontids (Therapsida : Cynodontia). *S Afr J Sci* **104**, 225-230 (2008); published online EpubMay-Jun (
10. S. Ray, A. Chinsamy, Diictodon feliceps (Therapsida, Dicynodontia): Bone histology, growth, and biomechanics. *J Vertebr Paleontol* **24**, 180-194 (2004); published online EpubMar (Doi 10.1671/1914-14).
11. J. R. Horner, Padian, K. & Ricqlès, A. d. , Comparative osteohistology of some embryonic and perinatal archosaurs: developmental and behavioral implications for dinosaurs. *Paleobiology* **27**, 39-58 (2001).
12. J.-S. Haines, The evolution of epiphyses and of endochondral bone. *Biological Review* **174**, 267-292 (1942).
13. P. M. Hughes, Rayner, J. M. V., Jones, G. , Ontogeny of 'true'flight and other aspects of growth in the bat Pipistrellus pipistrellus. *Journal of Zoology* **236**, 291-318 (1995).
14. L. V. Powers, Kandarian, S. C., Kunz, T. H. , Ontogeny of flight in the little brown bat, Myotis lucifugus: behavior, morphology, and muscle histochemistry. *Journal of Comparative Physiology A: Neuroethology, Sensory, Neural, and Behavioral Physiology* **168**, 675-685 (1991).
15. V. Elangovan, E. Yuvana Satya Priya, H. Raghuram, G. Marimuthu, Wing morphology and flight development in the short-nosed fruit bat Cynopterus sphinx. *Zoology (Jena)* **110**, 189-196 (2007)10.1016/j.zool.2007.02.001).
16. L. Wang, Lin, A., Xiao, Y., Jiang, T., Feng, J., Postnatal development in the big-footed bat, Myotis macrodactylus: wing morphology, echolocation calls, and flight. *Acta theriologica* **59**, 435-441 (2014).
17. R. A. Adams, Thibault, K. M. , Ontogeny and evolution of the hindlimb and calcar: assessing phylogenetic trends. *Ontogeny, functional ecology, and evolution of bats*, 316-332 (2000).
18. J. W. Hermanson, K. T. Wilkins, Growth and development of two species of bats in a shared maternity roost. *Cells Tissues Organs* **187**, 24-34 (2008)10.1159/000109961).

19. D. Koyabu, N. T. Son, Patterns of postcranial ossification and sequence heterochrony in bats: life histories and developmental trade-offs. *J Exp Zool B Mol Dev Evol* **322**, 607-618 (2014); published online EpubDec (10.1002/jez.b.22581).
20. T. H. Kunz, Hood, W. R. , Parental care and postnatal growth in the Chiroptera. *Reproductive biology of bats*, 415-468 (2000).
21. P. A. Racey, Entwistle, A. C. , Life-history and reproductive strategies of bats. *Reproductive biology of bats*, 363-414 (2000).
22. D. Eilam, G. Shefer, The developmental order of bipedal locomotion in the jerboa (Jaculus orientalis): pivoting, creeping, quadrupedalism, and bipedalism. *Developmental psychobiology* **31**, 137-142 (1997); published online EpubSep (
23. P. D. Gingerich, M. Ul-Haq, W. von Koenigswald, W. J. Sanders, B. H. Smith, I. S. Zalmout, New protocetid whale from the middle eocene of pakistan: birth on land, precocial development, and sexual dimorphism. *PLoS One* **4**, e4366 (2009)10.1371/journal.pone.0004366).
24. M. Uhen, Form, function, and anatomy of Dorudon atrox (Mammalia, Cetacea): an archaeocete from the middle to late Eocene of Egypt. *Papers on Paleontology* **34**, 1-222 (2004).
25. L. N. Cooper, Forelimb anatomy. *Encyclopedia of marine mammals, 2nd edition*, 449-452 (2009).
26. L. Mellor, Cooper, L. N., Torre, J., Brownell, Jr. R. L. , Paedomorphic ossification in porpoises with an emphasis on the vaquita (Phocoena sinus). *Aquatic Mammals* **35**, 193-202 (2009).
27. D. R. Carter, MikiĆ, B., Padian, K. , Epigenetic mechanical factors in the evolution of long bone epiphyses. *Zoological Journal of the Linnean Society* **123**, 163-178 (1998).
28. D. R. Carter, M. Wong, The role of mechanical loading histories in the development of diarthrodial joints. *J Orthop Res* **6**, 804-816 (1988)10.1002/jor.1100060604).
29. A. S. Chagin, E. Karimian, K. Sundstrom, E. Eriksson, L. Savendahl, Catch-up growth after dexamethasone withdrawal occurs in cultured postnatal rat metatarsal bones. *J Endocrinol* **204**, 21-29 (2010); published online EpubJan (10.1677/JOE-09-0307).
30. S. Dupont, L. Morsut, M. Aragona, E. Enzo, S. Giulitti, M. Cordenonsi, F. Zanconato, J. Le Digabel, M. Forcato, S. Bicciato, N. Elvassore, S. Piccolo, Role of YAP/TAZ in mechanotransduction. *Nature* **474**, 179-183 (2011); published online EpubJun 08 (10.1038/nature10137).
31. S. Strano, E. Munarriz, M. Rossi, L. Castagnoli, Y. Shaul, A. Sacchi, M. Oren, M. Sudol, G. Cesareni, G. Blandino, Physical interaction with Yes-associated protein enhances p73 transcriptional activity. *J Biol Chem* **276**, 15164-15173 (2001); published online EpubMay 04 (10.1074/jbc.M010484200).
32. H. P. Gerber, T. H. Vu, A. M. Ryan, J. Kowalski, Z. Werb, N. Ferrara, VEGF couples hypertrophic cartilage remodeling, ossification and angiogenesis during endochondral bone formation. *Nat Med* **5**, 623-628 (1999); published online EpubJun (10.1038/9467).
33. A. Karaca, V. R. Malladi, Y. Zhu, O. Tafaj, E. Paltrinieri, J. Y. Wu, Q. He, M. Bastepe, Constitutive stimulatory G protein activity in limb mesenchyme

1000 impairs bone growth. *Bone* **110**, 230-237 (2018); published online
1001 EpubMay (10.1016/j.bone.2018.02.016).
1002 34. S. Sasagawa, H. Takemori, T. Uebi, D. Ikegami, K. Hiramatsu, S. Ikegawa, H.
1003 Yoshikawa, N. Tsumaki, SIK3 is essential for chondrocyte hypertrophy
1004 during skeletal development in mice. *Development* **139**, 1153-1163
1005 (2012); published online EpubMar (10.1242/dev.072652).
1006 35. X. Xu, Z. Li, L. Cai, S. Calve, C. P. Neu, Mapping the Nonreciprocal
1007 Micromechanics of Individual Cells and the Surrounding Matrix Within
1008 Living Tissues. *Sci Rep* **6**, 24272 (2016); published online EpubApr 12
1009 (10.1038/srep24272).
1010 36. G. J. Breur, J. Turgai, B. A. Vanenkevort, C. E. Farnum, N. J. Wilsman,
1011 Stereological and serial section analysis of chondrocytic enlargement in the
1012 proximal tibial growth plate of the rat. *Anat Rec* **239**, 255-268 (1994);
1013 published online EpubJul (10.1002/ar.1092390304).
1014 37. N. J. Wilsman, C. E. Farnum, E. M. Leiferman, M. Fry, C. Barreto, Differential
1015 growth by growth plates as a function of multiple parameters of
1016 chondrocytic kinetics. *J Orthop Res* **14**, 927-936 (1996); published online
1017 EpubNov (10.1002/jor.1100140613).
1018 38. E. Kozhemyakina, A. B. Lassar, E. Zelzer, A pathway to bone: signaling
1019 molecules and transcription factors involved in chondrocyte development
1020 and maturation. *Development* **142**, 817-831 (2015); published online
1021 EpubMar 1 (10.1242/dev.105536).
1022 39. C. Barreto, R. M. Albrecht, D. E. Bjorling, J. R. Horner, N. J. Wilsman, Evidence
1023 of the growth plate and the growth of long bones in juvenile dinosaurs.
1024 *Science* **262**, 2020-2023 (1993); published online EpubDec 24
1025 (10.1126/science.262.5142.2020).
1026 40. C. T. Mehlman, A. Araghi, D. R. Roy, Hyphenated history: the Hueter-
1027 Volkmann law. *Am J Orthop (Belle Mead NJ)* **26**, 798-800 (1997); published
1028 online EpubNov (
1029 41. S. Sanchez, P. E. Ahlberg, K. M. Trinajstic, A. Mirone, P. Tafforeau, Three-
1030 dimensional synchrotron virtual paleohistology: a new insight into the
1031 world of fossil bone microstructures. *Microscopy and microanalysis : the*
1032 *official journal of Microscopy Society of America, Microbeam Analysis*
1033 *Society, Microscopical Society of Canada* **18**, 1095-1105 (2012); published
1034 online EpubOct (10.1017/S1431927612001079).
1035 42. D. Paganin, S. C. Mayo, T. E. Gureyev, P. R. Miller, S. W. Wilkins,
1036 Simultaneous phase and amplitude extraction from a single defocused
1037 image of a homogeneous object. *Journal of microscopy* **206**, 33-40 (2002);
1038 published online EpubApr (
1039 43. J. C. Labiche, O. Mathon, S. Pascarelli, M. A. Newton, G. G. Ferre, C. Curfs, G.
1040 Vaughan, A. Homs, D. F. Carreiras, Invited article: the fast readout low noise
1041 camera as a versatile x-ray detector for time resolved dispersive extended
1042 x-ray absorption fine structure and diffraction studies of dynamic
1043 problems in materials science, chemistry, and catalysis. *The Review of*
1044 *scientific instruments* **78**, 091301 (2007); published online EpubSep
1045 (10.1063/1.2783112).
1046 44. B. Jordan, P. Vercammen, K. L. Cooper, Husbandry and breeding of the
1047 lesser Egyptian Jerboa, Jaculus jaculus. *Cold Spring Harb Protoc* **2011**,

1048 1457-1461 (2011); published online EpubDec 1
1049 (10.1101/pdb.prot066712).
1050 45. J. Wallin, J. Wilting, H. Koseki, R. Fritsch, B. Christ, R. Balling, The role of Pax-
1051 1 in axial skeleton development. *Development* **120**, 1109-1121 (1994);
1052 published online EpubMay (
1053 46. D. A. Ovchinnikov, J. M. Deng, G. Ogunrinu, R. R. Behringer, Col2a1-directed
1054 expression of Cre recombinase in differentiating chondrocytes in
1055 transgenic mice. *Genesis* **26**, 145-146 (2000); published online EpubFeb (
1056 47. A. S. Chagin, K. K. Vuppalapati, T. Kobayashi, J. Guo, T. Hirai, M. Chen, S.
1057 Offermanns, L. S. Weinstein, H. M. Kronenberg, G-protein stimulatory
1058 subunit alpha and Gq/11alpha G-proteins are both required to maintain
1059 quiescent stem-like chondrocytes. *Nat Commun* **5**, 3673 (2014); published
1060 online EpubApr 30 (10.1038/ncomms4673).
1061